Engineering Analysis with Boundary Elements 192 (2026) 106957

Contents lists available at ScienceDirect

Engineering Analysis with Boundary Elements

journal homepage: www.elsevier.com/locate/enganabound

Dirichlet-type absorbing boundary conditions for ordinary state-based peridynamics

Alexander Hermann [a,*], Arman Shojaei [b], Christian J. Cyron [a,b]

[a] Institute for Artificial Intelligence and Simulation in Mechanics, Hamburg University of Technology, Eissendorfer Str. 42, 21073 Hamburg, Germany
[b] Institute of Material Systems Modeling, Helmholtz-Zentrum Hereon, Max–Planck-Str. 1, 21502 Geesthacht, Germany

ARTICLE INFO

Keywords:
Ordinary state-based peridynamics
Linear peridynamic solid
Unbounded domain
Absorbing boundary conditions
Discrete dispersion relation

ABSTRACT

We present time-domain Dirichlet-type absorbing boundary conditions (ABCs) for 2D ordinary state-based peridynamics using the Linear Peridynamic Solid (LPS) model, aimed at efficiently truncating unbounded elastodynamic domains while retaining the flexibility of arbitrary Poisson ratios. The proposed ABCs are built from a semi-analytical far-field representation expressed as a finite superposition of plane-wave modes satisfying the discrete LPS dispersion relation, so that outgoing waves are absorbed consistently with the numerical P- and S-wave branches and their Poisson-ratio-dependent polarizations. A cloud-based collocation and least-squares procedure eliminates the unknown modal amplitudes locally and yields precomputable updating operators that prescribe boundary displacement and velocity directly within explicit time stepping, avoiding spatial derivatives, transform techniques, auxiliary evolution equations, and surface-correction procedures at truncated horizons. Unlike our earlier bond-based ABC formulations, the present work requires a new state-based far-field theory, a new discrete dispersion operator with coupled P- and S-wave branches for general Poisson ratios, and an additional treatment of the nonlocal dilatation field. Numerical benchmarks show that the resulting ABCs strongly suppress nonphysical reflections over a broad range of material parameters, providing a simple and robust alternative to absorbing layers.

1. Introduction

Peridynamics is a nonlocal reformulation of continuum solid mechanics in which spatial derivatives are replaced by finite-horizon integral interactions, allowing the governing equations to remain well-defined in the presence of discontinuities such as cracks and evolving damage [1,2]. Beyond its original bond-based form, state-based peridynamics generalizes the constitutive description by allowing the material response at a point to depend collectively on the deformation of its neighborhood through peridynamic states [3,4]. This generality is essential for modeling realistic elastic behavior in reduced-dimensional settings, where bond-based models impose well-known restrictions on admissible Poisson ratios, while ordinary state-based formulations can accommodate the full range of elastic parameters required in applications [5]. The Linear Peridynamic Solid (LPS) model has become a widely used ordinary state-based specialization for linear elasticity, providing a convenient framework for wave propagation as well as for coupling to more complex inelastic mechanisms [6,7].

Accurate simulation of transient waves in unbounded or semi-infinite media is central to many problems in engineering and applied physics. Numerically, however, the computational domain must be truncated, which introduces artificial reflections unless special absorbing treatments are imposed at the truncation boundary. In classical wave modeling, this challenge has motivated a broad literature on absorbing boundary conditions (ABCs) and non-reflecting boundary conditions, including local approximations [8–12] and absorbing layers such as perfectly matched layers (PMLs) [13,14]. Transferring these ideas to peridynamics is nontrivial for several fundamental reasons: (1) the governing operator is a finite-horizon integral rather than a local differential operator, so standard derivations based on PDE factorization, characteristic variables, or local Dirichlet-to-Neumann maps do not carry over directly; (2) near an artificial boundary the horizon is truncated, meaning that particles in the near-boundary region interact with material that is no longer present, so any boundary treatment must address missing nonlocal interactions (often leading to fictitious-region constructions or correction strategies) [15–17]; (3) the boundary response is inherently nonlocal in space and may couple multiple directions within the horizon, making it difficult to impose a compact local relation that remains accurate for general incidence angles and wave types; (4) the use of transform-based operators (e.g., Fourier or Laplace techniques commonly employed to derive

* Corresponding author.
E-mail address: alexander.hermann@tuhh.de (A. Hermann).

https://doi.org/10.1016/j.enganabound.2026.106957
Received 12 March 2026; Received in revised form 22 June 2026; Accepted 5 August 2026
Available online 14 August 2026

non-reflecting conditions in local wave models) is not straightforward in peridynamics [18,19], because the nonlocal integral operator and finite horizon complicate the formulation and efficient evaluation of the resulting boundary symbols; and (5) even for linear elastic materials, peridynamic wave propagation is dispersive, so an absorbing treatment must be compatible with wavelength-dependent phase and group behavior rather than a single wave speed [19,20]. Moreover, the reflection behavior of a numerical peridynamic model is governed by its discrete dispersion characteristics, which can deviate substantially from continuum predictions and depend sensitively on the horizon size, discretization spacing, and time step, particularly when these scales are not well separated from the wavelengths of interest [20,21].

Several approaches have been proposed to mitigate boundary reflections in peridynamic computations. Absorbing-layer strategies have been developed in the peridynamic setting, most notably the PML formulation of Wildman and Gazonas for two-dimensional peridynamics, which leverages state-based constitutive flexibility to represent the anisotropic absorbing medium inherent to a PML construction [22]. In addition to absorbing layers, more "exact" artificial boundary operators have been derived for two-dimensional peridynamics, for example through constructions based on analytic representations and recursions, which can achieve high accuracy but may lead to boundary operators that are nonlocal in time and less convenient for explicit transient solvers [23].

Recently, Shojaei et al. proposed nonlocal Dirichlet-type absorbing boundary conditions for bond-based peridynamics in two-dimensional unbounded and semi-unbounded domains, formulated as time-dependent displacement and velocity prescriptions on an absorbing boundary layer [19]. The qualifier Dirichlet-type refers to how these conditions enter the scheme rather than to how their values are computed: the absorbing nodes are advanced by prescribing the kinematic field variables themselves, displacement and velocity, much as a classical Dirichlet condition prescribes the solution rather than its flux, and in contrast to a Neumann-type condition that would prescribe tractions. The modal far-field expansion only supplies these values and does not change their Dirichlet character. The boundary data are obtained from a semi-analytical far-field expansion composed of peridynamic plane-wave modes that satisfy the same numerical dispersion relations as the near-field discretization, ensuring compatibility between the truncated-domain solution and the outgoing-wave content generated by the discrete scheme. Because the construction is carried out directly in the time and space domains and acts only in the exterior absorbing layer, it can be readily combined with near-field nonlinearities and dynamic fracture processes, enabling simulations of crack initiation and propagation in otherwise unbounded settings while minimizing spurious reflections from the artificial boundary. This discrete-dispersion consistency is particularly appealing for peridynamic waves, since it targets the actual propagating content produced by the numerical scheme [20].

Despite this progress, ordinary state-based peridynamics introduces additional boundary-related challenges that are especially pronounced for elastodynamics. In LPS-type models, volumetric response is mediated through a nonlocal measure of dilatation computed from neighborhood data. Near truncated horizons, this volumetric measure can be biased by missing interactions, producing the so-called surface effect and motivating a variety of boundary-correction and fictitious-region strategies [15,16]. While such remedies can be effective in bounded-domain analyses, incorporating them into an absorbing treatment can complicate both analysis and implementation, and may blur whether residual reflections originate from imperfect absorption or from boundary-induced inconsistencies of the state-based kinematics. This difficulty is specific to state-based models and is precisely why a convincing absorbing treatment for LPS cannot be obtained by merely reusing the bond-based recipe. A successful construction must simultaneously handle wave absorption, discrete P–S mode coupling, and the boundary-consistent evolution of the nonlocal dilatation, which makes the present problem substantially more demanding both analytically and algorithmically.

The present work, inspired by [19,20,24], addresses these issues by developing time-domain, Dirichlet-type absorbing boundary conditions tailored to two-dimensional ordinary state-based peridynamic elastodynamics within the LPS framework. The central idea is to construct a semi-analytical far-field representation as a finite superposition of plane-wave modes that satisfy the discrete LPS dispersion relation, thereby capturing the compressional and shear branches and their dependence on Poisson ratio at the level relevant to the numerical near field. A cloud-based collocation and least-squares procedure is then used locally to eliminate the unknown modal amplitudes, yielding precomputable updating operators that prescribe boundary displacement and velocity directly during explicit time stepping. Because the absorbing-layer nodes are advanced through these Dirichlet-type updates rather than by enforcing the peridynamic equation of motion on a truncated neighborhood, the proposed construction is designed to avoid the need for additional surface-correction procedures within the absorbing treatment.

The resulting method offers a combination of features that is difficult to achieve with existing approaches: it applies directly to ordinary state-based elastodynamics with arbitrary Poisson ratios, it is compatible with the discrete dispersion of the numerical near field, it is implemented entirely in the time domain without transform techniques, and it avoids introducing extra boundary-correction machinery within the absorbing layer that could compromise robustness in transient simulations. These characteristics make the proposed ABCs a practical and conceptually clean route to domain truncation for state-based peridynamic wave propagation.

The present construction follows the same overall strategy as our earlier bond-based elastic ABCs [19]: the far field is represented by a superposition of plane-wave modes, the unknown modal amplitudes are eliminated locally by a cloud-based least-squares fit, and the resulting updating operators are precomputed and applied during explicit time stepping. Its state-based content, however, differs at every stage, and these differences share a common origin in the volumetric response of the state-based model, which couples dilatational and deviatoric deformation and is absent from the bond-based theory. This coupling enriches the underlying wave physics, so that the absorbing modes must now resolve compressional and shear branches whose speeds and polarizations vary with the Poisson ratio, in place of the single fixed branch structure of the bond-based case. It also brings into play a nonlocal measure of dilatation that has no bond-based counterpart and that must be transported consistently across the absorbing layer, which calls for an additional precomputed operator beyond those that update displacement and velocity. Finally, because the admissible time step and spatial sampling now depend on the Poisson ratio, they can no longer be fixed by hand in advance, as in the bond-based work, but are calibrated automatically during preprocessing. The bond-based ABCs are thereby recovered only in the special case of the single Poisson ratio for which this volumetric coupling vanishes, rather than reproduced by reformulation.

The remainder of this paper is organized as follows. Section 2 reviews the ordinary state-based peridynamic formulation, its meshfree discretization, and time integration. Section 3 defines the unbounded-domain problem and the absorbing-layer setting. Section 4 presents the proposed Dirichlet-type absorbing boundary conditions, including the LPS dispersion analysis, the discrete dispersion-consistent formulation, and the cloud-based far-field approximation. Section 5 describes the implementation and parameter selection. Section 6 provides numerical results. Section 7 summarizes the main findings.

2. Overview of ordinary state-based peridynamics and its meshfree discretization

In the peridynamic literature, two main classes of models are distinguished: bond-based peridynamics and state-based peridynamics [1,3].

In the present work we employ *ordinary state-based peridynamics*, which provides the constitutive flexibility required for linear elastodynamics with arbitrary Poisson ratios. This section summarizes the ordinary state-based peridynamic formulation and the meshfree (particle-based) discretization used throughout the paper. Let a body occupy a reference domain $\Omega \subset \mathbb{R}^2$ and be represented by material points with positions $\mathbf{x} = (x, y)$ and associated infinitesimal volumes $\mathrm{d}V_{\mathbf{x}}$. Each point $\mathbf{x} \in \Omega$ interacts with points in its finite neighborhood

$$\mathcal{H}_{\mathbf{x}} = \left\{ \mathbf{x}' \in \Omega : \|\mathbf{x}' - \mathbf{x}\| \le \delta \right\}, \tag{1}$$

where $\delta > 0$ denotes the peridynamic *horizon*, i.e., the characteristic length scale of nonlocal interactions. A motion is described by the deformation map $\mathbf{y}(\mathbf{x}, t) = \mathbf{x} + \mathbf{u}(\mathbf{x}, t)$, where $\mathbf{u}(\mathbf{x}, t)$ is the displacement vector field and t denotes time. For a pair of interacting points $\mathbf{x}$ and $\mathbf{x}' \in \mathcal{H}_{\mathbf{x}}$, we introduce the relative position (bond) vector $\boldsymbol{\xi} = \mathbf{x}' - \mathbf{x}$ (see Fig. 1). Following the state-based notation [3,4], kinematics are expressed through vector states acting on bonds: the reference position vector state is $\underline{\mathbf{X}}\langle\boldsymbol{\xi}\rangle = \boldsymbol{\xi}$, and the deformation vector state at $\mathbf{x}$ is

$$\underline{\mathbf{Y}}_{\mathbf{x}}\langle\boldsymbol{\xi}\rangle = \mathbf{y}(\mathbf{x} + \boldsymbol{\xi}, t) - \mathbf{y}(\mathbf{x}, t) = \boldsymbol{\xi} + \mathbf{u}(\mathbf{x} + \boldsymbol{\xi}, t) - \mathbf{u}(\mathbf{x}, t), \tag{2}$$

which measures the deformed separation of the interacting points. The associated scalar extension state is defined as

$$\underline{e}_{\mathbf{x}}\langle\boldsymbol{\xi}\rangle = \|\underline{\mathbf{Y}}_{\mathbf{x}}\langle\boldsymbol{\xi}\rangle\| - \|\boldsymbol{\xi}\|, \tag{3}$$

and it will be used below to define ordinary state-based constitutive relations via dilatation and deviatoric response.

The balance of linear momentum in ordinary state-based peridynamics is expressed through an integral equation of motion. Denoting by $\rho(\mathbf{x})$ the mass density and by $\mathbf{b}(\mathbf{x}, t)$ a prescribed body force density, the displacement field $\mathbf{u}(\mathbf{x}, t)$ satisfies

$$\rho(\mathbf{x})\,\ddot{\mathbf{u}}(\mathbf{x}, t) = \int_{\mathcal{H}_{\mathbf{x}}} \Big(\underline{\mathbf{T}}_{\mathbf{x}}\langle\mathbf{x}' - \mathbf{x}\rangle - \underline{\mathbf{T}}_{\mathbf{x}'}\langle\mathbf{x} - \mathbf{x}'\rangle \Big) \mathrm{d}V_{\mathbf{x}'} + \mathbf{b}(\mathbf{x}, t), \tag{4}$$

where $\underline{\mathbf{T}}_{\mathbf{x}}\langle\boldsymbol{\xi}\rangle$ is the *force vector state* at $\mathbf{x}$ that maps each bond vector $\boldsymbol{\xi} = \mathbf{x}' - \mathbf{x}$, with $\mathbf{x}' \in \mathcal{H}_{\mathbf{x}}$, to the force density per unit volume squared exerted by the material point $\mathbf{x}' = \mathbf{x} + \boldsymbol{\xi}$ on $\mathbf{x}$ [3,4]. In contrast to bond-based models, the state-based force state may depend on the collective deformation of the entire neighborhood through $\underline{\mathbf{Y}}_{\mathbf{x}}$, which provides the constitutive flexibility required for ordinary state-based elasticity.

For *ordinary* state-based materials, the peridynamic force vector state is assumed to be collinear with the deformed bond direction [3,4]. Introducing the relative displacement vector

$$\boldsymbol{\eta}(\mathbf{x}, \mathbf{x}', t) = \mathbf{u}(\mathbf{x}', t) - \mathbf{u}(\mathbf{x}, t), \tag{5}$$

the corresponding deformed bond vector is $\boldsymbol{\xi} + \boldsymbol{\eta}$, and the force state at $\mathbf{x}$ takes the form

$$\underline{\mathbf{T}}_{\mathbf{x}}\langle\boldsymbol{\xi}\rangle = \underline{t}_{\mathbf{x}}\langle\boldsymbol{\xi}\rangle \, \frac{\boldsymbol{\xi} + \boldsymbol{\eta}}{\|\boldsymbol{\xi} + \boldsymbol{\eta}\|}, \tag{6}$$

where $\underline{t}_{\mathbf{x}}\langle\boldsymbol{\xi}\rangle$ is a *scalar force state* (force magnitude per unit volume squared) that encodes the constitutive response through its dependence on the deformation state in the neighborhood of $\mathbf{x}$.

Throughout this work we adopt the *Linear Peridynamic Solid* (LPS) constitutive model, an ordinary state-based specialization for isotropic linear elasticity [3,4]. The model employs a radial, nonnegative *influence function* $\omega(|\xi|)$ and the associated *weighted volume*

$$m_{\mathbf{x}} = \int_{\mathcal{H}_{\mathbf{x}}} \omega(|\xi|)\, |\xi|^2 \, \mathrm{d}V_{\mathbf{x}'}, \tag{7}$$

The nonlocal volumetric strain measure is the *dilatation* $\theta(\mathbf{x}, t)$, defined in terms of the scalar extension state by

$$\theta(\mathbf{x}, t) = \frac{d}{m_{\mathbf{x}}} \int_{\mathcal{H}_{\mathbf{x}}} \omega(|\xi|)\, |\xi|\, \underline{e}_{\mathbf{x}}\langle\boldsymbol{\xi}\rangle \, \mathrm{d}V_{\mathbf{x}'}, \tag{8}$$

where d denotes the spatial dimension. The *deviatoric* part of the extension state is obtained by removing the volumetric contribution,

$$\underline{e}^{\mathrm{d}}_{\mathbf{x}}\langle\boldsymbol{\xi}\rangle = \underline{e}_{\mathbf{x}}\langle\boldsymbol{\xi}\rangle - \frac{\theta(\mathbf{x}, t)}{d}\, |\xi|, \tag{9}$$

and the LPS scalar force state is then given by

$$\underline{t}_{\mathbf{x}}\langle\boldsymbol{\xi}\rangle = \frac{d\,\kappa}{m_{\mathbf{x}}}\, \theta(\mathbf{x}, t)\, \omega(|\xi|)\, |\xi| + \alpha\, \omega(|\xi|)\, \underline{e}^{\mathrm{d}}_{\mathbf{x}}\langle\boldsymbol{\xi}\rangle, \tag{10}$$

with bulk modulus κ and deviatoric coefficient α specifying the material response.

In what follows we focus on small deformations about the reference configuration, for which the LPS model admits a convenient linearization that will be used repeatedly in subsequent developments. In particular, the extension state can be approximated by the projection of the relative displacement onto the reference bond direction,

$$\underline{e}_{\mathbf{x}}\langle\boldsymbol{\xi}\rangle = \|\boldsymbol{\xi} + \boldsymbol{\eta}\| - \|\boldsymbol{\xi}\| \;\approx\; \frac{\boldsymbol{\xi}}{\|\boldsymbol{\xi}\|} \cdot \boldsymbol{\eta}(\mathbf{x}, \mathbf{x}', t), \tag{11}$$

and the unit direction of the deformed bond satisfies $(\boldsymbol{\xi} + \boldsymbol{\eta})/\|\boldsymbol{\xi} + \boldsymbol{\eta}\| \approx \boldsymbol{\xi}/\|\boldsymbol{\xi}\|$. Consequently, the force vector state (6) becomes

$$\underline{\mathbf{T}}_{\mathbf{x}}\langle\boldsymbol{\xi}\rangle \;\approx\; \underline{t}_{\mathbf{x}}\langle\boldsymbol{\xi}\rangle \, \frac{\boldsymbol{\xi}}{\|\boldsymbol{\xi}\|}. \tag{12}$$

With (11), the dilatation (8) can be written in the linearized form

$$\theta(\mathbf{x}, t) \approx \frac{d}{m_{\mathbf{x}}} \int_{\mathcal{H}_{\mathbf{x}}} \omega(|\xi|)\, \boldsymbol{\xi} \cdot \boldsymbol{\eta}(\mathbf{x}, \mathbf{x}', t)\, \mathrm{d}V_{\mathbf{x}'}, \tag{13}$$

and the deviatoric extension state (9) becomes

$$\underline{e}^{\mathrm{d}}_{\mathbf{x}}\langle\boldsymbol{\xi}\rangle \approx \frac{\boldsymbol{\xi}}{\|\boldsymbol{\xi}\|} \cdot \boldsymbol{\eta}(\mathbf{x}, \mathbf{x}', t) - \frac{\theta(\mathbf{x}, t)}{d}\, \|\boldsymbol{\xi}\|. \tag{14}$$

For homogeneous materials and sufficiently interior points, $m_{\mathbf{x}}$ is constant (denoted m), and the parameters κ and α are chosen such that the local limit recovers the desired isotropic elastic response.

For the two-dimensional plane-strain setting considered in this work, the spatial dimension is $d = 2$ and the LPS parameters are chosen via the classical correspondence conditions so that the local limit recovers isotropic linear elasticity [3,4]. In particular, for a material with Young's modulus E, Poisson ratio ν, and density ρ, the Lamé parameters are

$$\lambda = \frac{E\nu}{(1+\nu)(1-2\nu)}, \qquad \mu = \frac{E}{2(1+\nu)}, \tag{15}$$

and the LPS constitutive coefficients are taken as

$$\kappa = \lambda + \mu, \qquad \alpha = \frac{8\mu}{m}, \tag{16}$$

where m denotes the weighted volume (7) for a representative interior point (constant for homogeneous materials away from boundaries). For a circular horizon with constant influence function $\omega(|\xi|) = 1$ in two dimensions, the corresponding continuum value evaluates to

$$m_{\mathrm{ref}} = \int_{\mathcal{H}_{\mathbf{x}}} |\xi|^2 \, \mathrm{d}V_{\mathbf{x}'} = \frac{\pi\delta^4}{2}, \tag{17}$$

and, on sufficiently regular discretizations, m approaches m_{ref}. For reference, the associated classical plane-strain wave speeds are $c_{\mathrm{P}} = \sqrt{(\lambda + 2\mu)/\rho}$ and $c_{\mathrm{S}} = \sqrt{\mu/\rho}$.

The elastic (strain) energy density of the LPS model is given by [3,4]

$$W(\mathbf{x}, t) = \frac{\kappa}{2}\, \theta(\mathbf{x}, t)^2 + \frac{\alpha}{2} \int_{\mathcal{H}_{\mathbf{x}}} \omega(|\mathbf{x}' - \mathbf{x}|) \big(\underline{e}^{\mathrm{d}}_{\mathbf{x}}\langle\mathbf{x}' - \mathbf{x}\rangle \big)^2 \mathrm{d}V_{\mathbf{x}'}, \tag{18}$$

and the corresponding kinetic energy density is $\frac{1}{2}\rho(\mathbf{x})\|\dot{\mathbf{u}}(\mathbf{x}, t)\|^2$. The total mechanical energy over $\Omega_E \subseteq \Omega$ is defined as

$$E_{\mathrm{tot}}(t) = \int_{\Omega_E} \Big(\frac{1}{2}\rho(\mathbf{x})\|\dot{\mathbf{u}}(\mathbf{x}, t)\|^2 + W(\mathbf{x}, t) \Big)\, \mathrm{d}V_{\mathbf{x}}. \tag{19}$$

The discrete evaluation employed in this work is introduced in the following subsection.

2.1. Meshfree discretization

The spatial discretization in peridynamics is commonly carried out with meshfree, particle-based methods [2,25–27]. Here, we adopt

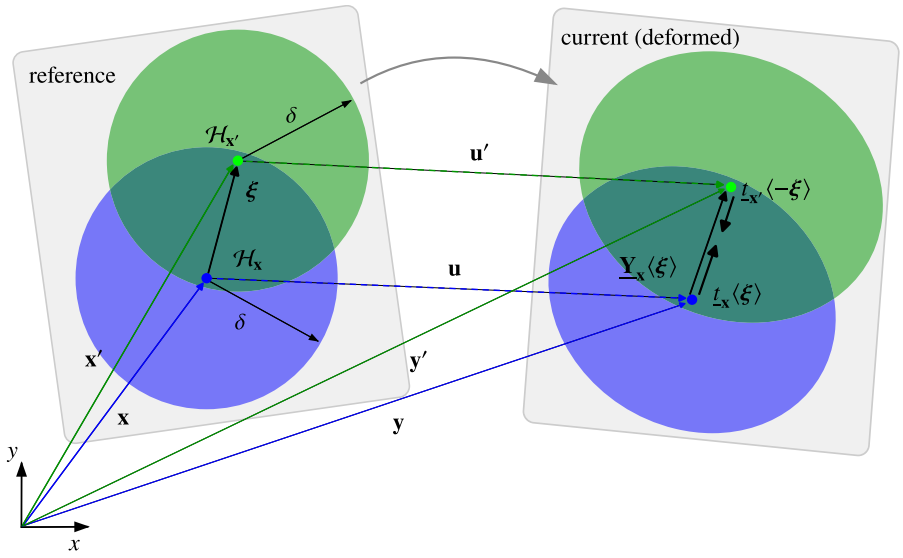

Fig. 1. Kinematics of ordinary state-based peridynamics: reference configuration and deformed configuration for a pair of interacting material points $\mathbf{x}$ and $\mathbf{x}' = \mathbf{x} + \boldsymbol{\xi}$ within the horizon $\mathcal{H}_{\mathbf{x}}$.

the standard meshfree discretization used in the peridynamic community [2]. The domain Ω is represented by a set of material points $\{\mathbf{x}_i\}_{i=1}^{N}$ placed on a uniform Cartesian lattice with spacing Δx (see Fig. 2). In two dimensions, each point is assigned a nodal volume (cell area) $V_i = \Delta V = (\Delta x)^2$. For a given point i, its family is

$$\mathcal{H}_i = \left\{ j \in \{1, \dots, N\} \setminus \{i\} \,:\, \|\mathbf{x}_j - \mathbf{x}_i\| \le \delta \right\}, \tag{20}$$

and the bond vector is $\boldsymbol{\xi}_{ij} = \mathbf{x}_j - \mathbf{x}_i$. Horizon integrals are approximated by particle quadrature with a *volume reduction factor* $\beta_{ij} = \beta(\boldsymbol{\xi}_{ij})$, which accounts for partial overlap of the family cell with the horizon near $|\boldsymbol{\xi}| = \delta$:

$$\int_{\mathcal{H}_{\mathbf{x}_i}} f(\mathbf{x}', \mathbf{x}_i)\, \mathrm{d}V_{\mathbf{x}'} \;\approx\; \sum_{j \in \mathcal{H}_i} f(\mathbf{x}_j, \mathbf{x}_i)\, \beta_{ij}\, V_j, \tag{21}$$

where we employ the standard piecewise definition in [28] as

$$\beta(\boldsymbol{\xi}) = \begin{cases} 1, & \|\boldsymbol{\xi}\| \le \delta - \dfrac{\Delta x}{2}, \\ \dfrac{\delta - \|\boldsymbol{\xi}\|}{\Delta x} + \dfrac{1}{2}, & \delta - \dfrac{\Delta x}{2} \le \|\boldsymbol{\xi}\| \le \delta + \dfrac{\Delta x}{2}, \\ 0, & \text{otherwise.} \end{cases} \tag{22}$$

The discrete kinematic measures are evaluated bondwise, e.g. $\underline{\mathbf{Y}}_i\langle\boldsymbol{\xi}_{ij}\rangle = \mathbf{y}_j - \mathbf{y}_i = \boldsymbol{\xi}_{ij} + \mathbf{u}_j - \mathbf{u}_i$ and $\underline{e}_i\langle\boldsymbol{\xi}_{ij}\rangle = \|\underline{\mathbf{Y}}_i\langle\boldsymbol{\xi}_{ij}\rangle\| - \|\boldsymbol{\xi}_{ij}\|$. With (21), the weighted volume and dilatation become

$$\begin{aligned} m_i &= \sum_{j \in \mathcal{H}_i} \omega(\|\boldsymbol{\xi}_{ij}\|)\, \|\boldsymbol{\xi}_{ij}\|^2\, \beta_{ij}\, V_j, \\ \theta_i &= \frac{d}{m_i} \sum_{j \in \mathcal{H}_i} \omega(\|\boldsymbol{\xi}_{ij}\|)\, \|\boldsymbol{\xi}_{ij}\|\, \underline{e}_i\langle\boldsymbol{\xi}_{ij}\rangle\, \beta_{ij}\, V_j, \end{aligned} \tag{23}$$

which are then used to evaluate the LPS scalar force state $\underline{t}_i\langle\boldsymbol{\xi}_{ij}\rangle$ via (10) (and hence the force vector state $\underline{\mathbf{T}}_i\langle\boldsymbol{\xi}_{ij}\rangle$). Finally, substituting (21) into (4) yields the spatially discrete equation of motion

$$\rho_i\, \ddot{\mathbf{u}}_i(t) = \sum_{j \in \mathcal{H}_i} \Big(\underline{\mathbf{T}}_i\langle\boldsymbol{\xi}_{ij}\rangle - \underline{\mathbf{T}}_j\langle\boldsymbol{\xi}_{ji}\rangle \Big) \beta_{ij}\, V_j + \mathbf{b}_i(t), \tag{24}$$

where $\rho_i = \rho(\mathbf{x}_i)$ and $\mathbf{b}_i(t) = \mathbf{b}(\mathbf{x}_i, t)$.

2.2. Time integration

Time is discretized into instants $t^0, t^1, \dots, t^n, t^{n+1}, \dots$ with constant time step $\Delta t = t^{n+1} - t^n$, so that $t^n = t^0 + n\Delta t$. We denote the nodal displacement, velocity, and acceleration at time t^n by $\mathbf{u}_i^n$, $\dot{\mathbf{u}}_i^n$, and $\ddot{\mathbf{u}}_i^n$, respectively. At each time level, the acceleration $\ddot{\mathbf{u}}_i^n$ is obtained from the spatially discrete peridynamic equation of motion (24) evaluated using the current nodal displacements $\{\mathbf{u}_k^n\}$.

For the explicit time marching we employ the velocity Verlet scheme [19]:

$$\dot{\mathbf{u}}_i^{\,n+\frac{1}{2}} = \dot{\mathbf{u}}_i^n + \frac{\Delta t}{2}\, \ddot{\mathbf{u}}_i^n, \tag{25}$$

$$\mathbf{u}_i^{n+1} = \mathbf{u}_i^n + \Delta t\, \dot{\mathbf{u}}_i^{\,n+\frac{1}{2}}, \tag{26}$$

$$\dot{\mathbf{u}}_i^{n+1} = \dot{\mathbf{u}}_i^{\,n+\frac{1}{2}} + \frac{\Delta t}{2}\, \ddot{\mathbf{u}}_i^{n+1}, \tag{27}$$

where $\ddot{\mathbf{u}}_i^{n+1}$ is computed after $\mathbf{u}_i^{n+1}$ has been predicted by (26). Equivalently, (25)–(27) can be written in the compact form

$$\mathbf{u}_i^{n+1} = \mathbf{u}_i^n + \Delta t\, \dot{\mathbf{u}}_i^n + \frac{\Delta t^2}{2}\, \ddot{\mathbf{u}}_i^n, \tag{28}$$

$$\dot{\mathbf{u}}_i^{n+1} = \dot{\mathbf{u}}_i^n + \frac{\Delta t}{2} \left(\ddot{\mathbf{u}}_i^n + \ddot{\mathbf{u}}_i^{n+1} \right). \tag{29}$$

The stability of the explicit scheme requires Δt to remain below a critical value Δt_c. As a conservative rule of thumb, one may choose Δt on the order of $\Delta x / c_{\mathrm{P}}$, where Δx is the characteristic particle spacing and c_{P} is the compressional wave speed. Further discussion and practical estimates for stability restrictions in peridynamic time integration can be found in [2,29].

3. Problem description

We consider the transient elastodynamic initial-value problem governed by the ordinary state-based peridynamic LPS model in an unbounded two-dimensional medium. For analysis and computation, the physical space is decomposed into a bounded *near field* Ω_{NF}, which contains the region of interest (e.g., sources, heterogeneities, or evolving damage), and an exterior *far field*

$$\Omega_{\mathrm{FF}} = \mathbb{R}^2 \setminus \overline{\Omega}_{\mathrm{NF}}, \tag{30}$$

which is assumed homogeneous, undamaged, and supports only outward-radiating wave motion. The interface $\Gamma_\infty = \partial\Omega_{\mathrm{NF}}$ is an *artificial boundary* introduced to truncate the unbounded problem to a computationally tractable domain (see Fig. 3).

Initial conditions are prescribed as $\mathbf{u}(\mathbf{x}, 0) = \mathbf{u}_0(\mathbf{x})$ and $\dot{\mathbf{u}}(\mathbf{x}, 0) = \mathbf{v}_0(\mathbf{x})$. When present, body forces $\mathbf{b}(\mathbf{x}, t)$ are confined to the near field so

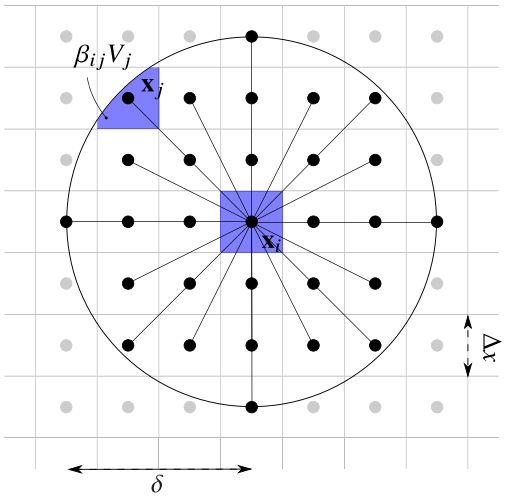

Fig. 2. Meshfree discretization of the peridynamic domain: a material point $\mathbf{x}_i$ interacts with all neighbors $\mathbf{x}_j$ in its family $\mathcal{H}_i$ (shaded region of radius δ).

that waves are generated inside Ω_{NF} and propagate outward into Ω_{FF}. Accordingly, Ω_{NF} is chosen such that

$$\mathrm{supp}(\mathbf{u}_0) \cup \mathrm{supp}(\mathbf{v}_0) \subset \Omega_{\mathrm{NF}}, \qquad \mathrm{supp}(\mathbf{b}(\cdot,t)) \subset \Omega_{\mathrm{NF}} \quad \text{for all } t \geq 0, \tag{31}$$

and the far field is initially at rest. Because peridynamic interactions act over a finite horizon δ, naively truncating the domain at Γ_∞ removes the nonlocal interactions coupling Ω_{NF} and Ω_{FF}, generating artificial reflections that contaminate the interior solution. To suppress these spurious reflections, we introduce an *absorbing layer* $\mathcal{A} \subset \Omega_{\mathrm{NF}}$, a layer of nodes adjacent to Γ_∞ with thickness at least δ, within which time-dependent Dirichlet data are prescribed so as to emulate propagation in an unbounded medium. The construction of such data for the LPS model is the subject of the following section.

4. Proposed method

The objective of this section is to derive time-domain Dirichlet-type absorbing boundary conditions for the LPS model. Following [19], we represent the far-field response by a finite superposition of outgoing peridynamic plane-wave modes and eliminate the corresponding modal amplitudes locally by a collocation procedure, which yields precomputable update vectors for displacement and velocity in the absorbing layer. In contrast to the bond-based setting, the LPS model involves the dilatation θ, which couples volumetric and deviatoric responses for general Poisson ratios. This coupling alters the underlying plane-wave dispersion analysis and requires a consistent evaluation of θ in the absorbing layer. The required ingredients are introduced in the following subsections. Accordingly, the methodological burden is substantially higher than in the previously published bond-based ABCs [19]: here the absorbing construction must reproduce not only the kinematics of outgoing waves but also their state-based volumetric content in a form that remains compatible with the discrete near-field solver.

4.1. LPS plane waves and dispersion relation

In the far field Ω_{FF}, the medium is homogeneous, the material remains undamaged, and displacements are small. The governing equation therefore reduces to the linearized LPS equation of motion without body forces. Using the linearized extension (11), the linearized deviatoric extension (14), and the linearized force-state direction (12), the scalar force state at $\mathbf{x}$ along the bond $\boldsymbol{\xi}$ can be written as

$$\underline{t}_{\mathbf{x}}\langle\boldsymbol{\xi}\rangle = \lambda_{\mathrm{PD}}\,\omega(|\boldsymbol{\xi}|)\,|\boldsymbol{\xi}|\,\theta(\mathbf{x},t) + \alpha\,\omega(|\boldsymbol{\xi}|)\,\big(\hat{\boldsymbol{\xi}}\cdot\boldsymbol{\eta}(\mathbf{x},\mathbf{x}+\boldsymbol{\xi},t)\big), \tag{32}$$

where $\hat{\boldsymbol{\xi}} = \boldsymbol{\xi}/|\boldsymbol{\xi}|$ and the dilatation coupling coefficient is

$$\lambda_{\mathrm{PD}} = \frac{d\,\kappa}{m} - \frac{\alpha}{d}. \tag{33}$$

Specializing to $d = 2$ under plane strain and substituting the correspondence relations (15) and (16) yields

$$\lambda_{\mathrm{PD}} = \frac{2(\lambda+\mu)}{m} - \frac{4\mu}{m} = \frac{2(\lambda-\mu)}{m}. \tag{34}$$

The coefficient λ_{PD} vanishes if and only if $\lambda = \mu$, which in plane strain corresponds to $\nu = 1/4$, i.e., the Poisson-ratio restriction of bond-based peridynamics. For all other admissible Poisson ratios, $\lambda_{\mathrm{PD}} \neq 0$ and the dilatation enters the force computation through a nontrivial volumetric coupling term. This coupling is the key structural difference between the LPS and bond-based settings that the present ABC construction must accommodate.

An analogous expression holds at the neighboring point $\mathbf{x}' = \mathbf{x} + \boldsymbol{\xi}$ along the opposite bond $-\boldsymbol{\xi}$. In the equation of motion (4), the internal-force contribution of the pair $(\mathbf{x},\mathbf{x}')$ enters through the difference $\underline{\mathbf{T}}_{\mathbf{x}}\langle\boldsymbol{\xi}\rangle - \underline{\mathbf{T}}_{\mathbf{x}'}\langle-\boldsymbol{\xi}\rangle$. Using the collinearity of the ordinary force state (6), the unit-direction relation $(-\boldsymbol{\xi})/\|-\boldsymbol{\xi}\| = -\hat{\boldsymbol{\xi}}$, and the antisymmetry $\boldsymbol{\eta}(\mathbf{x}',\mathbf{x},t) = -\boldsymbol{\eta}(\mathbf{x},\mathbf{x}',t)$, this difference can be written as

$$\begin{aligned}\underline{\mathbf{T}}_{\mathbf{x}}\langle\boldsymbol{\xi}\rangle - \underline{\mathbf{T}}_{\mathbf{x}'}\langle-\boldsymbol{\xi}\rangle = \omega(|\boldsymbol{\xi}|)\,\Big[\,&\lambda_{\mathrm{PD}}\,|\boldsymbol{\xi}|\big(\theta(\mathbf{x},t)+\theta(\mathbf{x}+\boldsymbol{\xi},t)\big)\\ &+2\alpha\,\hat{\boldsymbol{\xi}}\cdot\boldsymbol{\eta}(\mathbf{x},\mathbf{x}+\boldsymbol{\xi},t)\,\Big]\,\hat{\boldsymbol{\xi}}.\end{aligned} \tag{35}$$

Substituting (35) into (4) with $\mathbf{b} = \mathbf{0}$ yields the linearized far-field equation of motion

$$\begin{aligned}\rho\,\ddot{\mathbf{u}}(\mathbf{x},t) = \int_{\mathcal{H}_{\mathbf{x}}} \omega(|\boldsymbol{\xi}|)\,\Big[\,&\lambda_{\mathrm{PD}}\,|\boldsymbol{\xi}|\big(\theta(\mathbf{x},t)+\theta(\mathbf{x}+\boldsymbol{\xi},t)\big)\\ &+2\alpha\,\hat{\boldsymbol{\xi}}\cdot\boldsymbol{\eta}(\mathbf{x},\mathbf{x}+\boldsymbol{\xi},t)\,\Big]\,\hat{\boldsymbol{\xi}}\,\mathrm{d}V_{\mathbf{x}'}, \qquad \mathbf{x}\in\Omega_{\mathrm{FF}}.\end{aligned} \tag{36}$$

To construct a semi-analytical far-field solution, we seek plane-wave solutions of (36). Following [19], we consider complex-valued time-harmonic fields of the form

$$\boldsymbol{\psi}(\mathbf{x},t) = \boldsymbol{\gamma}\,\exp\big(\mathrm{i}\,\bar{\boldsymbol{\alpha}}\cdot\mathbf{x} + \mathrm{i}\,\bar{\omega}\,t\big), \qquad \boldsymbol{\gamma} = \begin{pmatrix}\gamma_1\\ \gamma_2\end{pmatrix}, \quad \|\boldsymbol{\gamma}\| = 1, \tag{37}$$

where $\mathrm{i} = \sqrt{-1}$ is the imaginary unit, $\bar{\boldsymbol{\alpha}} = (\bar{\alpha}_1,\bar{\alpha}_2) \in \mathbb{R}^2$ is the wave vector with magnitude $k = \|\bar{\boldsymbol{\alpha}}\|$ (wavenumber), $\bar{\omega} \in \mathbb{R}$ is the angular frequency, and $\boldsymbol{\gamma}$ is the polarization vector. Writing the wave vector in polar form as $\bar{\boldsymbol{\alpha}} = k(\cos\phi,\sin\phi)$ with $\phi \in (-\pi,\pi]$, the direction parameter ϕ spans all unit vectors on the circle and therefore accounts for plane-wave propagation in arbitrary directions in $\mathbb{R}^2$. The relative displacement follows directly from (5) as

$$\begin{aligned}\boldsymbol{\eta}(\mathbf{x},\mathbf{x}',t) &= \boldsymbol{\psi}(\mathbf{x}',t) - \boldsymbol{\psi}(\mathbf{x},t)\\ &= \boldsymbol{\gamma}\,\exp\big(\mathrm{i}\,\bar{\boldsymbol{\alpha}}\cdot\mathbf{x} + \mathrm{i}\,\bar{\omega}\,t\big)\Big[\exp\big(\mathrm{i}\,\bar{\boldsymbol{\alpha}}\cdot(\mathbf{x}'-\mathbf{x})\big) - 1\Big]\\ &= \boldsymbol{\gamma}\,\exp\big(\mathrm{i}\,\bar{\boldsymbol{\alpha}}\cdot\mathbf{x} + \mathrm{i}\,\bar{\omega}\,t\big)\Big[\exp\big(\mathrm{i}\,\bar{\boldsymbol{\alpha}}\cdot\boldsymbol{\xi}\big) - 1\Big].\end{aligned} \tag{38}$$

A key ingredient of (36), absent in bond-based peridynamics, is the dilatation θ. Substituting (38) into the linearized dilatation formula (13) gives

$$\theta(\mathbf{x},t) = \frac{d}{m}\,\exp\big(\mathrm{i}\,\bar{\boldsymbol{\alpha}}\cdot\mathbf{x} + \mathrm{i}\,\bar{\omega}\,t\big)\,\mathbf{S}(\bar{\boldsymbol{\alpha}})\cdot\boldsymbol{\gamma}, \tag{39}$$

where the sine integral vector $\mathbf{S}(\bar{\boldsymbol{\alpha}}) = (S_1(\bar{\boldsymbol{\alpha}}),S_2(\bar{\boldsymbol{\alpha}}))^{\mathrm{T}}$ has components

$$S_l(\bar{\boldsymbol{\alpha}}) = \int_{\mathcal{H}} \omega(|\boldsymbol{\xi}|)\,\xi_l\,\Big(\exp\big(\mathrm{i}\,\bar{\boldsymbol{\alpha}}\cdot\boldsymbol{\xi}\big) - 1\Big)\mathrm{d}V_{\xi}, \qquad l = 1,2, \tag{40}$$

with $\mathcal{H} = \{\boldsymbol{\xi}\in\mathbb{R}^2 : \|\boldsymbol{\xi}\| \leq \delta\}$ denoting the centered neighborhood. Since $\omega(|\boldsymbol{\xi}|)\,\xi_l$ is odd and $\cos(\bar{\boldsymbol{\alpha}}\cdot\boldsymbol{\xi}) - 1$ is even on the symmetric domain $\mathcal{H}$, the real part of S_l vanishes, and $\mathbf{S}(\bar{\boldsymbol{\alpha}})$ is purely imaginary. Equivalently,

$$S_l(\bar{\boldsymbol{\alpha}}) = \mathrm{i}\int_{\mathcal{H}} \omega(|\boldsymbol{\xi}|)\,\xi_l\,\sin\big(\bar{\boldsymbol{\alpha}}\cdot\boldsymbol{\xi}\big)\,\mathrm{d}V_{\xi} \;\in\; \mathrm{i}\,\mathbb{R}. \tag{41}$$

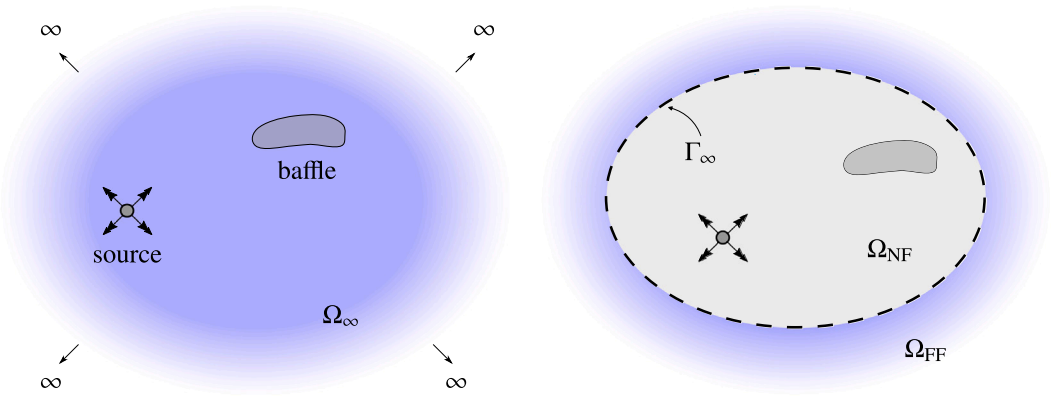

Fig. 3. Domain decomposition for the unbounded problem: the near field Ω_{NF} is enclosed by the artificial boundary Γ_∞, beyond which lies the homogeneous far field Ω_{FF}.

Introducing the dilatation amplitude $\hat{\theta} = \mathbf{S}(\bar{\boldsymbol{\alpha}}) \cdot \boldsymbol{\gamma}$, the sum of dilatations at $\mathbf{x}$ and $\mathbf{x} + \boldsymbol{\xi}$ becomes

$$\theta(\mathbf{x}, t) + \theta(\mathbf{x} + \boldsymbol{\xi}, t) = \frac{d}{m}\, \hat{\theta}\, \exp\!\big(\mathrm{i}\, \bar{\boldsymbol{\alpha}} \cdot \mathbf{x} + \mathrm{i}\, \bar{\omega}\, t\big) \Big(1 + \exp\!\big(\mathrm{i}\, \bar{\boldsymbol{\alpha}} \cdot \boldsymbol{\xi}\big)\Big). \tag{42}$$

Substituting (38) and (42) into (36) and canceling the common factor $\exp\!\big(\mathrm{i}\, \bar{\boldsymbol{\alpha}} \cdot \mathbf{x} + \mathrm{i}\, \bar{\omega}\, t\big)$, the jth component of the momentum balance separates into a deviatoric and a volumetric contribution. The deviatoric term, $2\alpha\, \omega(|\boldsymbol{\xi}|)\, (\hat{\boldsymbol{\xi}} \cdot \boldsymbol{\eta})\, \hat{\xi}_j$, yields

$$2\alpha \sum_{l=1}^{2} N_{jl}(\bar{\boldsymbol{\alpha}})\, \gamma_l, \tag{43}$$

where the deviatoric matrix $\mathbf{N}(\bar{\boldsymbol{\alpha}}) \in \mathbb{R}^{2\times 2}$ is defined by

$$N_{jl}(\bar{\boldsymbol{\alpha}}) = -\int_{\mathcal{H}} \frac{\omega(|\boldsymbol{\xi}|)\, \xi_j \xi_l}{|\boldsymbol{\xi}|^2} \Big(1 - \cos(\bar{\boldsymbol{\alpha}} \cdot \boldsymbol{\xi})\Big) \mathrm{d}V_\xi, \qquad j, l = 1, 2. \tag{44}$$

For a radial influence function on the symmetric neighborhood $\mathcal{H}$, $\mathbf{N}(\bar{\boldsymbol{\alpha}})$ is real and symmetric. Moreover, since $1 - \cos(\cdot) \geq 0$, the representation in (44) shows that $\mathbf{N}(\bar{\boldsymbol{\alpha}})$ is negative semidefinite. The second contribution, associated with the dilatation term $\lambda_{\mathrm{PD}}\, \omega(|\boldsymbol{\xi}|)\, |\boldsymbol{\xi}| \big(\theta(\mathbf{x}, t) + \theta(\mathbf{x} + \boldsymbol{\xi}, t)\big) \hat{\xi}_j$, requires the integral

$$\begin{aligned} &\int_{\mathcal{H}} \omega(|\boldsymbol{\xi}|)\, \xi_j \Big(1 + \exp\!\big(\mathrm{i}\, \bar{\boldsymbol{\alpha}} \cdot \boldsymbol{\xi}\big)\Big) \mathrm{d}V_\xi \\ &\quad = \int_{\mathcal{H}} \omega(|\boldsymbol{\xi}|)\, \xi_j\, \mathrm{d}V_\xi + \int_{\mathcal{H}} \omega(|\boldsymbol{\xi}|)\, \xi_j\, \exp\!\big(\mathrm{i}\, \bar{\boldsymbol{\alpha}} \cdot \boldsymbol{\xi}\big) \mathrm{d}V_\xi \\ &\quad = S_j(\bar{\boldsymbol{\alpha}}), \end{aligned} \tag{45}$$

where the first integral vanishes by symmetry of the centered neighborhood $\mathcal{H}$. The jth component of the dilatation contribution is therefore

$$\frac{d\, \lambda_{\mathrm{PD}}}{m} \sum_{l=1}^{2} S_j(\bar{\boldsymbol{\alpha}})\, S_l(\bar{\boldsymbol{\alpha}})\, \gamma_l. \tag{46}$$

This term has the structure of a rank-one operator proportional to $\mathbf{S}(\bar{\boldsymbol{\alpha}})\mathbf{S}(\bar{\boldsymbol{\alpha}})^{\mathrm{T}}$ acting on $\boldsymbol{\gamma}$. Since $S_j(\bar{\boldsymbol{\alpha}}) \in \mathrm{i}\,\mathbb{R}$ for $j = 1, 2$, the products $S_j S_l$ are real, so the dispersion matrix is real.

Equating the sum of (43) and (46) to the inertia term $-\rho\, \bar{\omega}^2 \boldsymbol{\gamma}$ yields the LPS dispersion eigenvalue problem

$$\Big(\mathbf{M}^{\mathrm{LPS}}(\bar{\boldsymbol{\alpha}}) + \rho\, \bar{\omega}^2 \mathbf{I}\Big) \boldsymbol{\gamma} = \mathbf{0}, \tag{47}$$

where $\mathbf{I}$ is the 2×2 identity matrix and the LPS dispersion matrix has components

$$M_{jl}^{\mathrm{LPS}}(\bar{\boldsymbol{\alpha}}) = \frac{d\, \lambda_{\mathrm{PD}}}{m}\, S_j(\bar{\boldsymbol{\alpha}})\, S_l(\bar{\boldsymbol{\alpha}}) + 2\alpha\, N_{jl}(\bar{\boldsymbol{\alpha}}), \qquad j, l = 1, 2. \tag{48}$$

The matrix $\mathbf{M}^{\mathrm{LPS}}(\bar{\boldsymbol{\alpha}})$ is real and symmetric. The appearance of the additional rank-one volumetric term is one of the core novelties of the present work: the state-based absorbing basis must be derived from this enriched operator, whereas the earlier bond-based ABCs [19] involved only the deviatoric-type contribution. For $d = 2$, the independent components are

$$\begin{aligned} M_{11}^{\mathrm{LPS}}(\bar{\boldsymbol{\alpha}}) &= \frac{2\lambda_{\mathrm{PD}}}{m}\, S_1^2(\bar{\boldsymbol{\alpha}}) + 2\alpha\, N_{11}(\bar{\boldsymbol{\alpha}}), \\ M_{12}^{\mathrm{LPS}}(\bar{\boldsymbol{\alpha}}) &= \frac{2\lambda_{\mathrm{PD}}}{m}\, S_1(\bar{\boldsymbol{\alpha}})\, S_2(\bar{\boldsymbol{\alpha}}) + 2\alpha\, N_{12}(\bar{\boldsymbol{\alpha}}), \\ M_{22}^{\mathrm{LPS}}(\bar{\boldsymbol{\alpha}}) &= \frac{2\lambda_{\mathrm{PD}}}{m}\, S_2^2(\bar{\boldsymbol{\alpha}}) + 2\alpha\, N_{22}(\bar{\boldsymbol{\alpha}}), \end{aligned} \tag{49}$$

with $M_{21}^{\mathrm{LPS}} = M_{12}^{\mathrm{LPS}}$ by symmetry. The dispersion condition

$$\det\Big(\mathbf{M}^{\mathrm{LPS}}(\bar{\boldsymbol{\alpha}}) + \rho\, \bar{\omega}^2 \mathbf{I}\Big) = 0 \tag{50}$$

yields four roots $\bar{\omega} = \pm\bar{\omega}_{\mathrm{P}}(\bar{\boldsymbol{\alpha}})$ and $\bar{\omega} = \pm\bar{\omega}_{\mathrm{S}}(\bar{\boldsymbol{\alpha}})$, where

$$\bar{\omega}_{\mathrm{P}}(\bar{\boldsymbol{\alpha}}) = \sqrt{\frac{-\lambda_1}{\rho}}, \qquad \bar{\omega}_{\mathrm{S}}(\bar{\boldsymbol{\alpha}}) = \sqrt{\frac{-\lambda_2}{\rho}}, \qquad 0 \leq \bar{\omega}_{\mathrm{S}} \leq \bar{\omega}_{\mathrm{P}}, \tag{51}$$

and $\lambda_1 \leq \lambda_2 \leq 0$ are the eigenvalues of $\mathbf{M}^{\mathrm{LPS}}(\bar{\boldsymbol{\alpha}})$ with corresponding normalized eigenvectors $\boldsymbol{\gamma}^{\mathrm{P}}$ and $\boldsymbol{\gamma}^{\mathrm{S}}$. The associated plane-wave modes are

$$\boldsymbol{\psi}^{\mathrm{P}}(\mathbf{x}, t) = \boldsymbol{\gamma}^{\mathrm{P}} \exp\!\big(\mathrm{i}\, \bar{\boldsymbol{\alpha}} \cdot \mathbf{x} \pm \mathrm{i}\, \bar{\omega}_{\mathrm{P}}\, t\big), \quad \boldsymbol{\psi}^{\mathrm{S}}(\mathbf{x}, t) = \boldsymbol{\gamma}^{\mathrm{S}} \exp\!\big(\mathrm{i}\, \bar{\boldsymbol{\alpha}} \cdot \mathbf{x} \pm \mathrm{i}\, \bar{\omega}_{\mathrm{S}}\, t\big). \tag{52}$$

In the long-wavelength limit $k\delta \to 0$ (vanishing nonlocality), the LPS dispersion relation recovers the classical plane-strain elastic relations, $\lim_{k\delta\to 0} \bar{\omega}_{\mathrm{P}}/k = c_{\mathrm{P}}$ and $\lim_{k\delta\to 0} \bar{\omega}_{\mathrm{S}}/k = c_{\mathrm{S}}$; the derivation is given in Appendix A.

4.2. Discrete dispersion relation and consistency with the near field

The dispersion analysis in the previous subsection is formulated in the continuum setting, where the integrals defining $\mathbf{S}(\bar{\boldsymbol{\alpha}})$ and $\mathbf{N}(\bar{\boldsymbol{\alpha}})$ are evaluated over the continuous neighborhood $\mathcal{H}$. As discussed in detail in [19,20], constructing far-field modes from these continuum-level integrals generally leads to a mismatch with the waves produced by a meshfree peridynamic discretization: particle quadrature replaces horizon integrals by weighted sums, so the resulting numerical model follows a discretization-dependent dispersion relation that can deviate noticeably from the analytical one, especially at larger wavenumbers. Using continuum modes in the absorbing layer would therefore introduce a systematic incompatibility at the truncation and generate artificial reflections.

To eliminate this inconsistency, $\mathbf{S}(\bar{\boldsymbol{\alpha}})$ and $\mathbf{N}(\bar{\boldsymbol{\alpha}})$ are evaluated using exactly the same discrete quadrature as in the near-field solver. Importantly, these discrete integrals are assembled for a *representative interior* node i whose family $\mathcal{H}_i$ forms a complete circular neighborhood (i.e., the horizon is not truncated). As a result, the corresponding plane-wave modes are calibrated with respect to a full, unbiased horizon

integration, and therefore represent the propagation characteristics of the numerical scheme in regions free of truncation-induced surface effects. This choice is essential here because the far-field representation is intended to approximate the solution as if it were embedded in an infinite medium with complete neighborhoods. For the present state-based setting, this discrete matching is even more critical than in the earlier bond-based ABC work [19,20], because any mismatch would contaminate not only the phase of the outgoing waves but also the volumetric contribution carried by the dilatation-dependent term in the LPS operator. For such an interior node i, with family $\mathcal{H}_i$ and volume reduction factors $\{\beta_{ij}\}$, the discrete counterparts of (40) and (44) are

$$S_l(\bar{\boldsymbol{\alpha}}) = \sum_{j\in\mathcal{H}_i} \omega(\|\boldsymbol{\xi}_{ij}\|)\,(\xi_{ij})_l\Big(\exp\big(\mathrm{i}\,\bar{\boldsymbol{\alpha}}\cdot\boldsymbol{\xi}_{ij}\big)-1\Big)\beta_{ij}V_j, \qquad l=1,2, \tag{53}$$

$$N_{pq}(\bar{\boldsymbol{\alpha}}) = -\sum_{j\in\mathcal{H}_i} \frac{\omega(\|\boldsymbol{\xi}_{ij}\|)\,(\xi_{ij})_p(\xi_{ij})_q}{\|\boldsymbol{\xi}_{ij}\|^2}\Big(1-\cos\big(\bar{\boldsymbol{\alpha}}\cdot\boldsymbol{\xi}_{ij}\big)\Big)\beta_{ij}V_j, \qquad p,q=1,2. \tag{54}$$

Using the corresponding discrete weighted volume $m = m_i$ defined in (23), the discrete LPS dispersion matrix becomes

$$M^{\mathrm{LPS}}_{pq}(\bar{\boldsymbol{\alpha}}) = \frac{d\,\lambda_{\mathrm{PD}}}{m}\,S_p(\bar{\boldsymbol{\alpha}})\,S_q(\bar{\boldsymbol{\alpha}}) + 2\alpha\,N_{pq}(\bar{\boldsymbol{\alpha}}), \qquad p,q=1,2, \tag{55}$$

and the eigenvalue problem (47) is solved using (53)–(55). Henceforth, **S**, **N**, and $\mathbf{M}^{\mathrm{LPS}}$ refer to these discrete evaluations. By construction, the resulting P- and S-wave modes satisfy the same numerical dispersion as the near-field discretization [19,20]. This discrete consistency is central for suppressing reflections; in particular, for LPS it directly controls the volumetric contribution through the rank-one term S_pS_q in (55).

Fig. 4 compares the dispersion behavior of the three relevant models: the classical local continuum, the continuous LPS relation of Section 4.1 (evaluated here in closed form), and the discrete LPS relation of the present scheme at three grid resolutions $\delta/\Delta x \in \{2,4,8\}$. For each branch the phase-velocity ratio $c/c_0 = \bar{\omega}/(c_0k)$ is plotted against the dimensionless wavenumber $k\delta$, using the branch-specific long-wavelength speed $c_0 = c_{\mathrm{P}}$ for the compressional and $c_0 = c_{\mathrm{S}}$ for the shear branch, so that every classical branch collapses onto the line $c/c_0 \equiv 1$ and the departure from it isolates the dispersion. Both peridynamic relations soften appreciably with increasing $k\delta$, a direct consequence of the finite horizon [1,30]. With the present quadrature and volume correction, coarsening the grid increases this softening deviation from the continuum: the $\delta/\Delta x = 2$ relation departs most, $\delta/\Delta x = 4$ is closer, and $\delta/\Delta x = 8$ is visually indistinguishable from the continuous closed form, each discrete curve being shown only up to its own grid Nyquist limit $k\delta = \pi\,\delta/\Delta x$. The discrete relation is moreover only weakly anisotropic; for $\delta/\Delta x = 4$ the axial ($\phi = 0$) and diagonal ($\phi = \pi/4$) propagation directions differ by less than about 3% even near the Nyquist limit. Taken together, this confirms that the present discretization faithfully reproduces the continuum LPS dispersion as the grid is refined. Since the propagating content of the numerical model follows this discrete relation rather than the classical or the continuous one, the absorbing modes are built from the discrete dispersion; using the classical or even the continuous relation would misrepresent the outgoing waves and seed spurious reflections.

The figure also reflects the strongly dispersive character of the model: both branches soften appreciably with $k\delta$, the longitudinal (P) branch falling further below unity than the transverse (S) one, so that, relative to their respective long-wavelength speeds, the P branch softens the more strongly. On the symmetry axis $\phi = 0$ the two modes are exactly longitudinal and transverse, and the branches are labeled accordingly by polarization.

4.3. Far-field solution

Let us consider a portion of the computational domain in the vicinity of the artificial boundary, as sketched in Fig. 5. The absorbing layer $\mathcal{A}$ consists of all nodes $\mathbf{x}_i$ whose distance to Γ_∞ does not exceed the horizon δ. To each absorbing node $\mathbf{x}_i \in \mathcal{A}$ we associate a circular neighborhood, referred to as the *cloud*, centered at $\mathbf{x}_i$ with radius δ,

$$C_i = \{\, j \;:\; \|\mathbf{x}_j - \mathbf{x}_i\| \le \delta \,\}. \tag{56}$$

Within C_i, the far-field displacement is locally approximated by a finite superposition of LPS plane-wave modes obtained from the dispersion analysis in Sections 4.1 and 4.2. The number of nodes in the cloud is denoted by $N_c = |C_i|$.

As depicted in Fig. 5, a local Cartesian coordinate system $(\bar{x},\bar{y})$ is associated with each cloud, with origin at $\mathbf{x}_i$. The local system is oriented so that the $\bar{x}$-axis is normal to Γ_∞ with positive direction towards the far field. The coordinates of a node $\mathbf{x}$ in this local system are found by the rotation matrix $\mathbf{T}(\tau)$ as

$$\bar{\mathbf{x}} = \mathbf{T}(\tau)\,(\mathbf{x}-\mathbf{x}_i), \qquad \mathbf{T}(\tau) = \begin{bmatrix} \cos\tau & -\sin\tau \\ \sin\tau & \cos\tau \end{bmatrix}, \tag{57}$$

where τ is the rotation angle from the global x-axis to the local $\bar{x}$-axis, as depicted in Fig. 5. This frame-rotation angle τ, which orients the local axes of the center node along the outward (radial) normal, is distinct from the propagation angle ϕ of the outgoing plane-wave half-spaces introduced below (Fig. 6), which is swept about that normal; both, in turn, differ from the physical incidence angle of the wavefront.

From the dispersion analyses in Sections 4.1 and 4.2, the discrete LPS dispersion relation admits two wave branches. For a wavenumber $k > 0$ and propagation direction $\phi \in (-\pi,\pi]$, with wave vector $\bar{\boldsymbol{\alpha}} = k(\cos\phi,\sin\phi)$, the corresponding plane-wave modes (cf. (52)) can be written as

$$\boldsymbol{\psi}^{\mathrm{P},\pm}(\mathbf{x},t;k,\phi) = \boldsymbol{\gamma}^{\mathrm{P}}(k,\phi)\,\exp\Big(\mathrm{i}\,k\big(\bar{x}\cos\phi+\bar{y}\sin\phi\big)\pm\mathrm{i}\,\bar{\omega}_{\mathrm{P}}(k,\phi)\,t\Big), \tag{58a}$$

$$\boldsymbol{\psi}^{\mathrm{S},\pm}(\mathbf{x},t;k,\phi) = \boldsymbol{\gamma}^{\mathrm{S}}(k,\phi)\,\exp\Big(\mathrm{i}\,k\big(\bar{x}\cos\phi+\bar{y}\sin\phi\big)\pm\mathrm{i}\,\bar{\omega}_{\mathrm{S}}(k,\phi)\,t\Big), \tag{58b}$$

where $\bar{\omega}_{\mathrm{P}}(k,\phi) > \bar{\omega}_{\mathrm{S}}(k,\phi) > 0$. The polarization vector $\boldsymbol{\gamma}^{\mathrm{P}}(k,\phi)$ is predominantly aligned with $\bar{\boldsymbol{\alpha}}$ (pressure mode), whereas $\boldsymbol{\gamma}^{\mathrm{S}}(k,\phi)$ is predominantly orthogonal to $\bar{\boldsymbol{\alpha}}$ (shear mode). The symbol $\pm$ indicates the two time-harmonic factors and will be selected below to enforce the outgoing-wave requirement.

To approximate the far-field displacement over a cloud C_i, we sample n_ϕ propagation directions $\{\phi_p\}_{p=1}^{n_\phi} \subset (-\pi,\pi]$ and n_k wavenumbers $\{k_q\}_{q=1}^{n_k} \subset (0,\infty)$. Introducing local coordinates $\bar{\mathbf{x}} = \mathbf{T}(\tau)(\mathbf{x}-\mathbf{x}_i)$ and the phase variable

$$\zeta_p = \bar{\mathbf{x}}\cdot(\cos\phi_p,\sin\phi_p) = \bar{x}\cos\phi_p + \bar{y}\sin\phi_p, \tag{59}$$

the far-field displacement is approximated as the modal superposition

$$\begin{aligned}\hat{\mathbf{u}}(\mathbf{x},t) = \sum_{p=1}^{n_\phi}\sum_{q=1}^{n_k}\Big[\,& a_{pq}\,\boldsymbol{\gamma}^{\mathrm{P}}_{pq}\,\exp\big(\mathrm{i}\,k_q\,\zeta_p - \mathrm{i}\,\bar{\omega}_{\mathrm{P},pq}\,t\big)\\ &+ b_{pq}\,\boldsymbol{\gamma}^{\mathrm{S}}_{pq}\,\exp\big(\mathrm{i}\,k_q\,\zeta_p - \mathrm{i}\,\bar{\omega}_{\mathrm{S},pq}\,t\big)\\ &+ c_{pq}\,\boldsymbol{\gamma}^{\mathrm{P}}_{pq}\,\exp\big(\mathrm{i}\,k_q\,\zeta_p + \mathrm{i}\,\bar{\omega}_{\mathrm{P},pq}\,t\big)\\ &+ d_{pq}\,\boldsymbol{\gamma}^{\mathrm{S}}_{pq}\,\exp\big(\mathrm{i}\,k_q\,\zeta_p + \mathrm{i}\,\bar{\omega}_{\mathrm{S},pq}\,t\big)\,\Big],\end{aligned} \tag{60}$$

where a_{pq}, b_{pq}, c_{pq}, and d_{pq} are unknown coefficients, $\boldsymbol{\gamma}^{\mathrm{P}}_{pq} = \boldsymbol{\gamma}^{\mathrm{P}}(k_q,\phi_p)$, $\boldsymbol{\gamma}^{\mathrm{S}}_{pq} = \boldsymbol{\gamma}^{\mathrm{S}}(k_q,\phi_p)$, and $\bar{\omega}_{\mathrm{P},pq} = \bar{\omega}_{\mathrm{P}}(k_q,\phi_p)$, $\bar{\omega}_{\mathrm{S},pq} = \bar{\omega}_{\mathrm{S}}(k_q,\phi_p)$. The total number of sampled wave vectors is $n_\phi n_k$. Note that the scalar phase variable ζ_p in (59) is defined in the local coordinate frame of node i and is distinct from the relative displacement $\boldsymbol{\eta}$ introduced in (5).

In (60), the far-field approximation includes both wave branches (P and S) and all sampled propagation directions, together with the two time-harmonic factors. For the absorbing construction, only those modes that transport energy from the near field into the exterior domain are retained. With the convention adopted in (58), the factors $\exp\big(\mathrm{i}\,k_q\,\zeta_p - \mathrm{i}\,\bar{\omega}_{\mathrm{P},pq}\,t\big)$ and $\exp\big(\mathrm{i}\,k_q\,\zeta_p - \mathrm{i}\,\bar{\omega}_{\mathrm{S},pq}\,t\big)$ (with $\bar{\omega}_{\mathrm{P},pq} > 0$, $\bar{\omega}_{\mathrm{S},pq} > 0$, and $k_q > 0$) correspond to propagation in the direction $\mathbf{n}(\phi_p) = (\cos\phi_p,\sin\phi_p)$, whereas the factors with $+\mathrm{i}\,\bar{\omega}\,t$ correspond to

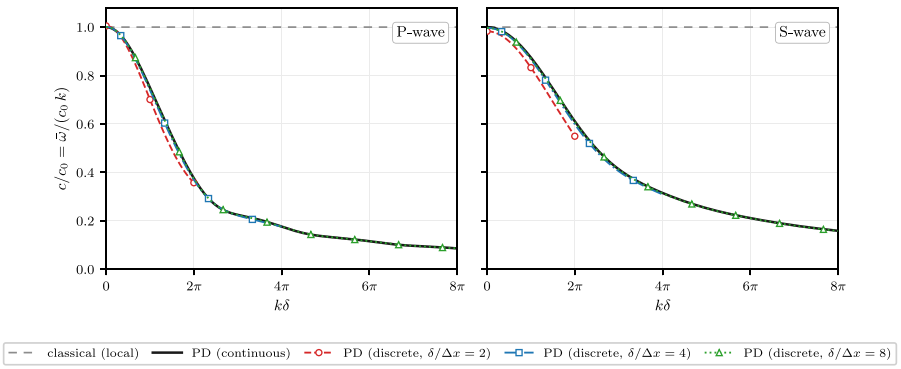

Fig. 4. Dispersion of the two-dimensional LPS model ($\nu = 0.30$, plane strain, constant influence function $\omega(|\xi|) \equiv 1$): phase-velocity ratio $c/c_0 = \bar{\omega}/(c_0 k)$ versus dimensionless wavenumber $k\delta$ for the compressional (P, $c_0 = c_P$) and shear (S, $c_0 = c_S$) branches. Three models are compared: the classical local continuum ($c/c_0 \equiv 1$), the continuous LPS relation evaluated in closed form, and the discrete LPS relation of the present scheme at three resolutions $\delta/\Delta x \in \{2, 4, 8\}$ (propagation along $\phi = 0$). Each discrete curve is shown up to its own grid Nyquist limit $k\delta = \pi\,\delta/\Delta x$, and converges to the continuum relation as $\delta/\Delta x$ increases. In the units $\mu = \rho = 1$, one has $c_S = 1$ and $c_P = 1.87$ as $k \to 0$. Branches are labeled by polarization (P, longitudinal; S, transverse).

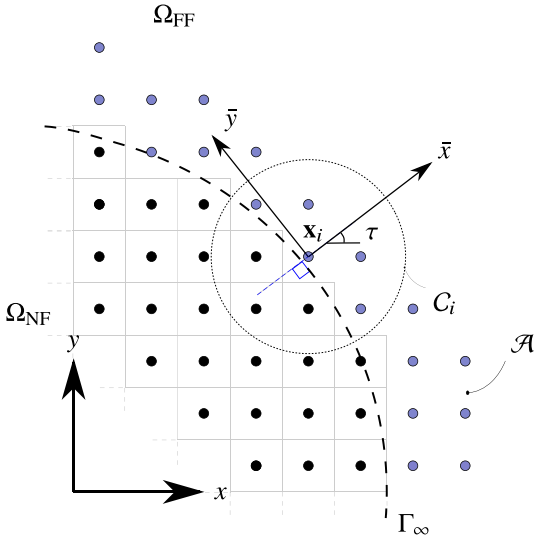

Fig. 5. Schematic of the absorbing layer $\mathcal{A}$ near the artificial boundary Γ_∞. For each absorbing node $\mathbf{x}_i$, the cloud C_i collects neighboring nodes within radius δ. The local frame $(\bar{x}, \bar{y})$ at $\mathbf{x}_i$, obtained by rotating the global axes through the angle τ, has its $\bar{x}$-axis along the outward normal.

propagation in the opposite direction $-\mathbf{n}(\phi_p)$. Since the latter represent incoming content from the exterior, they are excluded by setting

$$c_{pq} = d_{pq} = 0. \tag{61}$$

Accordingly, (60) reduces to the outgoing-wave representation

$$\hat{\mathbf{u}}(\mathbf{x}, t) = \sum_{p=1}^{n_\phi} \sum_{q=1}^{n_k} \Big[a_{pq}\, \boldsymbol{\gamma}^{\mathrm{P}}_{pq}\, \exp\big(\mathrm{i}\, k_q\, \zeta_p - \mathrm{i}\, \bar{\omega}^{\mathrm{P}}_{pq}\, t\big) + b_{pq}\, \boldsymbol{\gamma}^{\mathrm{S}}_{pq}\, \exp\big(\mathrm{i}\, k_q\, \zeta_p - \mathrm{i}\, \bar{\omega}^{\mathrm{S}}_{pq}\, t\big) \Big]. \tag{62}$$

Writing the local coordinates in polar form as $(\bar{x}, \bar{y}) = \varrho(\cos\vartheta, \sin\vartheta)$ with $\varrho \geq 0$ and $-\pi \leq \vartheta \leq \pi$, the phase variable satisfies $\zeta_p = \bar{x}\cos\phi_p + \bar{y}\sin\phi_p = \varrho\cos(\vartheta - \phi_p)$, and (62) becomes

$$\begin{aligned} \hat{\mathbf{u}}(\mathbf{x}, t) = \sum_{p=1}^{n_\phi} \sum_{q=1}^{n_k} \Big[& a_{pq}\, \boldsymbol{\gamma}^{\mathrm{P}}_{pq}\, \exp\big(\mathrm{i}\, k_q\, \varrho\cos(\vartheta - \phi_p) - \mathrm{i}\, \bar{\omega}^{\mathrm{P}}_{pq}\, t\big) \\ & + b_{pq}\, \boldsymbol{\gamma}^{\mathrm{S}}_{pq}\, \exp\big(\mathrm{i}\, k_q\, \varrho\cos(\vartheta - \phi_p) - \mathrm{i}\, \bar{\omega}^{\mathrm{S}}_{pq}\, t\big) \Big]. \end{aligned} \tag{63}$$

For fixed ϕ_p, the outgoing representation (63) is used on the half-space in which the phase variable is positive, i.e.,

$$\cos(\vartheta - \phi_p) > 0, \quad \text{equivalently,} \quad -\tfrac{\pi}{2} + \phi_p < \vartheta < \tfrac{\pi}{2} + \phi_p. \tag{64}$$

Condition (64) defines, for each sampled direction ϕ_p, an outward-oriented half-space through $\mathbf{x}_i$ in the local coordinate system. As illustrated in Fig. 6, varying ϕ_p rotates this half-space about $\mathbf{x}_i$ and thereby changes the range of incidence angles represented by the outgoing basis. In the implementation, we sample directions symmetrically as $\phi_p \in [-\Delta\phi, \Delta\phi]$, so that the mode set covers waves reaching the absorbing layer with moderate obliquity relative to the outward normal. We stress that $\Delta\phi$ is the angular aperture of the outgoing plane-wave basis in *phase* direction, measured about each node's local outward normal, and not the physical incidence angle of the wavefront: in the dispersive peridynamic medium the direction along which energy actually arrives is the group-velocity direction, which in general differs from the phase direction. Because the basis at each node is oriented along that node's local normal and represents only the locally outgoing half-space, a modest aperture suffices; the construction need not span all incidence angles globally, but only reproduce the outgoing content seen locally. The parameter $\Delta\phi$ should therefore be interpreted as a small angular aperture rather than as an attempt to span all directions: if chosen too large, some sampled modes no longer represent genuinely outgoing content and may redirect energy back toward the near field. The admissible range of $\Delta\phi$ is therefore bounded above. Rather than fixing the aperture from prior experience, we determine it directly from the non-amplification requirement of the updating operators; this analysis is carried out for the present discretization in Example 1 (Section 6), where the largest admissible aperture is found to be essentially material-independent, and all computations in this work use a value comfortably within it. By contrast, Δk controls the highest wavenumber represented in the basis and hence the spectral bandwidth of the far-field approximation. To remain compatible with the discrete lattice, it must satisfy the sampling bound $\Delta k \leq \pi/\Delta x$. In the present work the time step Δt is held at the explicit-integration (CFL) limit; for a fixed aperture, the aperture is then balanced against the wavenumber sampling Δk, the pair $(\Delta t, \Delta k)$ being selected systematically in Section 5 through the preprocessing sweep that balances stability and absorption quality.

To determine the unknown modal coefficients in the outgoing representation (62) from the known nodal values in the cloud, we employ a collocation procedure in a weighted least-squares sense, following [19, 31,32]. Displacements and velocities are approximated independently over the cloud. To this end, we introduce the local time coordinate $\bar{t} = t - t^n$, so that $\bar{t} \in [-\Delta t, \Delta t]$ on the time window centered at the current level t^n. Let

$$n_b = 2\, n_\phi n_k$$

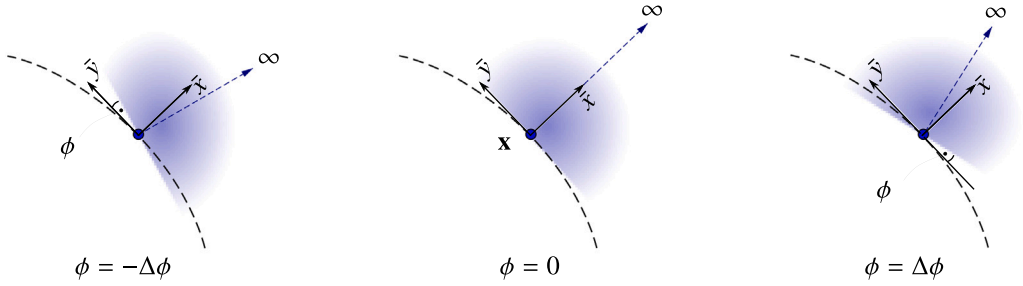

Fig. 6. Angular sampling of the outgoing plane-wave modes at an absorbing node $\mathbf{x}_i$. In the local frame $(\bar{x}, \bar{y})$, whose $\bar{x}$-axis points along the outward normal to Γ_∞, the propagation angle ϕ of the half-spaces is swept over the aperture $\phi \in [-\Delta\phi, \Delta\phi]$. This angle differs from the frame-rotation angle τ of Fig. 5 and from the physical incidence angle of the wavefront.

denote the total number of outgoing modes (P and S for each sampled wave vector). The displacement and velocity fields within C_i are approximated as

$$\hat{\mathbf{u}}^n(\mathbf{x}, t) = \mathbf{T}^{\mathrm{T}}(\tau)\,\boldsymbol{\Psi}(\bar{\mathbf{x}}, \bar{t})\,\mathbf{p}^n, \qquad \mathbf{x} \in C_i, \quad -\Delta t \le \bar{t} \le \Delta t, \tag{65}$$

$$\hat{\dot{\mathbf{u}}}^n(\mathbf{x}, t) = \mathbf{T}^{\mathrm{T}}(\tau)\,\dot{\boldsymbol{\Psi}}(\bar{\mathbf{x}}, \bar{t})\,\mathbf{q}^n, \qquad \mathbf{x} \in C_i, \quad -\Delta t \le \bar{t} \le \Delta t, \tag{66}$$

where $\bar{\mathbf{x}} = \mathbf{T}(\tau)(\mathbf{x} - \mathbf{x}_i)$ are local coordinates, $\mathbf{T}^{\mathrm{T}}(\tau)$ maps vectors from the local frame back to the global frame, $\boldsymbol{\Psi}$ and $\dot{\boldsymbol{\Psi}}$ are $2 \times n_b$ matrices collecting the basis functions and their time derivatives, and $\mathbf{p}^n, \mathbf{q}^n \in \mathbb{C}^{n_b}$ are vectors of unknown coefficients. Since (65) and (66) are constructed independently, $\mathbf{p}^n$ and $\mathbf{q}^n$ are not constrained to coincide. Each index $m = 1, \dots, n_b$ corresponds to one outgoing mode (either P or S) associated with one sampled pair (k, ϕ), and we denote by $\zeta_m = \bar{x}\cos\phi_m + \bar{y}\sin\phi_m$ the corresponding phase variable in the local coordinates. With this convention,

$$\boldsymbol{\Psi}(\bar{\mathbf{x}}, \bar{t}) = \Big[\boldsymbol{\gamma}_1\, e^{\mathrm{i}(k_1\zeta_1 - \bar{\omega}_1\bar{t})},\ \boldsymbol{\gamma}_2\, e^{\mathrm{i}(k_2\zeta_2 - \bar{\omega}_2\bar{t})},\ \dots,\ \boldsymbol{\gamma}_{n_b}\, e^{\mathrm{i}(k_{n_b}\zeta_{n_b} - \bar{\omega}_{n_b}\bar{t})}\Big], \tag{67}$$

$$\dot{\boldsymbol{\Psi}}(\bar{\mathbf{x}}, \bar{t}) = \Big[-\mathrm{i}\bar{\omega}_1\,\boldsymbol{\gamma}_1\, e^{\mathrm{i}(k_1\zeta_1 - \bar{\omega}_1\bar{t})},\ -\mathrm{i}\bar{\omega}_2\,\boldsymbol{\gamma}_2\, e^{\mathrm{i}(k_2\zeta_2 - \bar{\omega}_2\bar{t})},\ \dots,\ -\mathrm{i}\bar{\omega}_{n_b}\,\boldsymbol{\gamma}_{n_b}\, e^{\mathrm{i}(k_{n_b}\zeta_{n_b} - \bar{\omega}_{n_b}\bar{t})}\Big], \tag{68}$$

and

$$\mathbf{p}^n = \big(p_1^n,\ p_2^n,\ \dots,\ p_{n_b}^n\big)^{\mathrm{T}}, \qquad \mathbf{q}^n = \big(q_1^n,\ q_2^n,\ \dots,\ q_{n_b}^n\big)^{\mathrm{T}}. \tag{69}$$

Since an explicit time-marching scheme is employed, at time level t^n the nodal displacements and velocities at t^n and t^{n-1} are available. For an absorbing node $\mathbf{x}_i \in \mathcal{A}$, we collect the corresponding cloud data into the vectors

$$\bar{\mathbf{U}}^n = \begin{pmatrix} \mathbf{u}_{j_1}^n \\ \mathbf{u}_{j_1}^{n-1} \\ \vdots \\ \mathbf{u}_{j_{N_c}}^n \\ \mathbf{u}_{j_{N_c}}^{n-1} \end{pmatrix}, \qquad \bar{\mathbf{V}}^n = \begin{pmatrix} \dot{\mathbf{u}}_{j_1}^n \\ \dot{\mathbf{u}}_{j_1}^{n-1} \\ \vdots \\ \dot{\mathbf{u}}_{j_{N_c}}^n \\ \dot{\mathbf{u}}_{j_{N_c}}^{n-1} \end{pmatrix}, \qquad \{\mathbf{x}_{j_r}\}_{r=1}^{N_c} = C_i, \tag{70}$$

where $\mathbf{u}_j^n = (u_{j,x}^n, u_{j,y}^n)^{\mathrm{T}}$ and $\dot{\mathbf{u}}_j^n = (\dot{u}_{j,x}^n, \dot{u}_{j,y}^n)^{\mathrm{T}}$ are the displacement and velocity at node $\mathbf{x}_j$ and time t^n. Each of the vectors $\bar{\mathbf{U}}^n$ and $\bar{\mathbf{V}}^n$ has length $4N_c$. Evaluating the approximations (65)–(66) at the cloud nodes and at the two time offsets $\bar{t} = 0$ (time level t^n) and $\bar{t} = -\Delta t$ (time level t^{n-1}), and stacking the resulting equations in the same order as (70), yields the overdetermined linear systems

$$\bar{\mathbf{U}}^n \approx \mathbf{A}_u\,\mathbf{p}^n, \qquad \bar{\mathbf{V}}^n \approx \mathbf{A}_v\,\mathbf{q}^n, \tag{71}$$

with moment matrices

$$\mathbf{A}_u = \begin{bmatrix} \mathbf{T}^{\mathrm{T}}(\tau)\,\boldsymbol{\Psi}(\bar{\mathbf{x}}_{j_1}, 0) \\ \mathbf{T}^{\mathrm{T}}(\tau)\,\boldsymbol{\Psi}(\bar{\mathbf{x}}_{j_1}, -\Delta t) \\ \vdots \\ \mathbf{T}^{\mathrm{T}}(\tau)\,\boldsymbol{\Psi}(\bar{\mathbf{x}}_{j_{N_c}}, 0) \\ \mathbf{T}^{\mathrm{T}}(\tau)\,\boldsymbol{\Psi}(\bar{\mathbf{x}}_{j_{N_c}}, -\Delta t) \end{bmatrix}, \quad \mathbf{A}_v = \begin{bmatrix} \mathbf{T}^{\mathrm{T}}(\tau)\,\dot{\boldsymbol{\Psi}}(\bar{\mathbf{x}}_{j_1}, 0) \\ \mathbf{T}^{\mathrm{T}}(\tau)\,\dot{\boldsymbol{\Psi}}(\bar{\mathbf{x}}_{j_1}, -\Delta t) \\ \vdots \\ \mathbf{T}^{\mathrm{T}}(\tau)\,\dot{\boldsymbol{\Psi}}(\bar{\mathbf{x}}_{j_{N_c}}, 0) \\ \mathbf{T}^{\mathrm{T}}(\tau)\,\dot{\boldsymbol{\Psi}}(\bar{\mathbf{x}}_{j_{N_c}}, -\Delta t) \end{bmatrix}. \tag{72}$$

Each block $\mathbf{T}^{\mathrm{T}}(\tau)\,\boldsymbol{\Psi}(\bar{\mathbf{x}}_j, \bar{t})$ (and similarly for $\dot{\boldsymbol{\Psi}}$) has size $2 \times n_b$, hence $\mathbf{A}_u, \mathbf{A}_v \in \mathbb{C}^{4N_c \times n_b}$. Provided that $4N_c > n_b$, the systems (71) are solved in the least-squares sense using the Moore–Penrose pseudoinverse,

$$\mathbf{p}^n = \mathbf{A}_u^+\,\bar{\mathbf{U}}^n, \qquad \mathbf{q}^n = \mathbf{A}_v^+\,\bar{\mathbf{V}}^n. \tag{73}$$

Substituting (73) into (65)–(66) and evaluating at the cloud center $\bar{\mathbf{x}} = \bar{\mathbf{0}}$ and at $\bar{t} = \Delta t$ yields the Dirichlet-type updates for the absorbing node at time t^{n+1},

$$\mathbf{u}_i^{n+1} \approx \Re\Big\{\mathbf{T}^{\mathrm{T}}(\tau)\,\boldsymbol{\Psi}(\bar{\mathbf{0}}, \Delta t)\,\mathbf{A}_u^+\,\bar{\mathbf{U}}^n\Big\} = \Re\big\{\mathbf{G}_u^{(i)}\,\bar{\mathbf{U}}^n\big\}, \tag{74}$$

$$\dot{\mathbf{u}}_i^{n+1} \approx \Re\Big\{\mathbf{T}^{\mathrm{T}}(\tau)\,\dot{\boldsymbol{\Psi}}(\bar{\mathbf{0}}, \Delta t)\,\mathbf{A}_v^+\,\bar{\mathbf{V}}^n\Big\} = \Re\big\{\mathbf{G}_v^{(i)}\,\bar{\mathbf{V}}^n\big\}, \tag{75}$$

where the updating operators

$$\mathbf{G}_u^{(i)} = \mathbf{T}^{\mathrm{T}}(\tau)\,\boldsymbol{\Psi}(\bar{\mathbf{0}}, \Delta t)\,\mathbf{A}_u^+, \qquad \mathbf{G}_v^{(i)} = \mathbf{T}^{\mathrm{T}}(\tau)\,\dot{\boldsymbol{\Psi}}(\bar{\mathbf{0}}, \Delta t)\,\mathbf{A}_v^+ \tag{76}$$

have size $2 \times 4N_c$. The superscript (i) labels the absorbing node to which the operators belong: the rotation $\mathbf{T}(\tau)$, the moment matrices $\mathbf{A}_u$ and $\mathbf{A}_v$, and the cloud data are all formed from the cloud and local frame of node i, so every absorbing node carries its own operators $\mathbf{G}_u^{(i)}$ and $\mathbf{G}_v^{(i)}$. These operators prescribe displacement and velocity directly and do not involve spatial differentiation. Since the mode set, cloud geometry, and local coordinate frame are time-independent, $\mathbf{G}_u^{(i)}$ and $\mathbf{G}_v^{(i)}$ are precomputed once and reused; advancing an absorbing node then requires only two matrix–vector multiplications per time step (followed by taking the real part).

In the LPS model, the dilatation θ_i enters the force density through the volumetric coupling coefficient λ_{PD} (cf. (32)) and must therefore be available at all nodes prior to the force assembly. For interior nodes, θ_i is evaluated by discrete quadrature over the full family $\mathcal{H}_i$ (cf. (23)). For absorbing nodes, however, the horizon is truncated at the artificial boundary so that $\mathcal{H}_i$ is incomplete, and the quadrature-based dilatation suffers from the surface-effect bias in the volumetric contribution. To avoid this inconsistency, we prescribe θ_i in the absorbing layer from the same plane-wave far-field representation used to construct the Dirichlet updates, and we evaluate m (and hence $\alpha = 8\mu/m$ and λ_{PD}) using the same representative interior weighted volume employed in Section 4.2. This additional step is a decisive conceptual departure from the earlier bond-based ABCs [19]: the absorbing layer must now transport a state variable that is itself nonlocal, history-dependent through the cloud data, and directly coupled to the force balance. Consider an outgoing plane-wave mode of the form

$$\boldsymbol{\psi}(\mathbf{x}, t) = \boldsymbol{\gamma}\,\exp\big(\mathrm{i}\,\bar{\boldsymbol{\alpha}}\cdot\mathbf{x} - \mathrm{i}\,\bar{\omega}\,t\big).$$

Substituting this ansatz into the linearized dilatation relation (13) and following the derivation in Section 4.1 (cf. (39)) yields

$$\theta(\mathbf{x}, t) = \frac{d}{m}\,\big(\mathbf{S}(\bar{\boldsymbol{\alpha}})\cdot\boldsymbol{\gamma}\big)\,\exp\big(\mathrm{i}\,\bar{\boldsymbol{\alpha}}\cdot\mathbf{x} - \mathrm{i}\,\bar{\omega}\,t\big). \tag{77}$$

Thus, the dilatation associated with a plane-wave displacement mode shares the same oscillatory factor, with the vector amplitude $\boldsymbol{\gamma}$ replaced

by the scalar amplitude $(d/m)\,\mathbf{S}(\bar{\boldsymbol{\alpha}})\cdot\boldsymbol{\gamma}$. Since $\mathbf{S}(\bar{\boldsymbol{\alpha}})$ is purely imaginary (cf. (41)), this scalar amplitude lies in $\mathrm{i}\,\mathbb{R}$. Accordingly, for each outgoing mode $\ell = 1,\dots,n_b$ with wave vector $\bar{\boldsymbol{\alpha}}_\ell$, polarization $\boldsymbol{\gamma}_\ell$, wavenumber k_ℓ, phase variable ζ_ℓ, and frequency $\bar{\omega}_\ell$, we define the associated scalar dilatation basis function

$$\Theta_\ell(\bar{\mathbf{x}},\bar{t}) = \frac{d}{m}\left(\mathbf{S}(\bar{\boldsymbol{\alpha}}_\ell)\cdot\boldsymbol{\gamma}_\ell\right)\exp\!\big(\mathrm{i}\,(k_\ell\,\zeta_\ell - \bar{\omega}_\ell\,\bar{t})\big), \tag{78}$$

which is paired with the ℓth displacement mode. Collecting these functions yields the row vector $\boldsymbol{\Theta}(\bar{\mathbf{x}},\bar{t})\in\mathbb{C}^{1\times n_b}$,

$$\boldsymbol{\Theta}(\bar{\mathbf{x}},\bar{t}) = \big[\,\Theta_1(\bar{\mathbf{x}},\bar{t}),\ \Theta_2(\bar{\mathbf{x}},\bar{t}),\ \dots,\ \Theta_{n_b}(\bar{\mathbf{x}},\bar{t})\,\big]. \tag{79}$$

We approximate the dilatation within the cloud by

$$\theta^n(\mathbf{x},t) = \boldsymbol{\Theta}(\bar{\mathbf{x}},\bar{t})\,\mathbf{r}^n, \qquad \mathbf{x}\in C_i, \tag{80}$$

where $\mathbf{r}^n\in\mathbb{C}^{n_b}$ is a vector of unknown coefficients. No additional modes are introduced; the dilatation is represented by the same mode set used for the displacement and velocity updates. At time level t^n, the dilatation values θ_j^n and θ_j^{n-1} at cloud nodes $\mathbf{x}_j\in C_i$ are available from the preceding force evaluation. We collect them into the data vector

$$\boldsymbol{\Theta}^n = \begin{pmatrix} \theta^n_{j_1} \\ \theta^{n-1}_{j_1} \\ \vdots \\ \theta^n_{j_{N_c}} \\ \theta^{n-1}_{j_{N_c}} \end{pmatrix}, \qquad \{\mathbf{x}_{j_r}\}_{r=1}^{N_c} = C_i, \tag{81}$$

which has length $2N_c$. Evaluating (80) at all cloud nodes at $\bar{t}=0$ and $\bar{t}=-\Delta t$ yields the least-squares system

$$\boldsymbol{\Theta}^n \approx \mathbf{A}_\theta\,\mathbf{r}^n, \tag{82}$$

with the moment matrix $\mathbf{A}_\theta\in\mathbb{C}^{2N_c\times n_b}$ assembled as

$$\mathbf{A}_\theta = \begin{bmatrix} \boldsymbol{\Theta}(\bar{\mathbf{x}}_{j_1},0) \\ \boldsymbol{\Theta}(\bar{\mathbf{x}}_{j_1},-\Delta t) \\ \vdots \\ \boldsymbol{\Theta}(\bar{\mathbf{x}}_{j_{N_c}},0) \\ \boldsymbol{\Theta}(\bar{\mathbf{x}}_{j_{N_c}},-\Delta t) \end{bmatrix}. \tag{83}$$

The coefficients follow from the Moore–Penrose pseudoinverse,

$$\mathbf{r}^n = \mathbf{A}_\theta^+\,\boldsymbol{\Theta}^n. \tag{84}$$

Finally, evaluating (80) at the cloud center $\bar{\mathbf{x}}=\bar{\mathbf{0}}$ and at $\bar{t}=\Delta t$ gives the dilatation update

$$\theta_i^{n+1} \approx \Re\Big\{\boldsymbol{\Theta}(\bar{\mathbf{0}},\Delta t)\,\mathbf{A}_\theta^+\,\boldsymbol{\Theta}^n\Big\} = \Re\big\{\mathbf{G}_\theta^{(i)}\,\boldsymbol{\Theta}^n\big\}, \tag{85}$$

where

$$\mathbf{G}_\theta^{(i)} = \boldsymbol{\Theta}(\bar{\mathbf{0}},\Delta t)\,\mathbf{A}_\theta^+ \ \in\ \mathbb{C}^{1\times 2N_c} \tag{86}$$

is the (precomputable) dilatation updating row. As for $\mathbf{G}_u^{(i)}$ and $\mathbf{G}_v^{(i)}$, this operator is time-independent; at each time step, prescribing θ_i^{n+1} requires only a single row–vector multiplication (followed by taking the real part). The updated values θ_i^{n+1} are assigned to all absorbing nodes prior to the subsequent force evaluation, so that the volumetric coupling through λ_{PD} within the absorbing layer is driven by far-field wave content consistent with the outgoing discrete dispersion relation.

The three precomputed updating relations

$$\mathbf{u}_i^{n+1} \approx \Re\big\{\mathbf{G}_u^{(i)}\,\bar{\mathbf{U}}^n\big\}, \qquad \dot{\mathbf{u}}_i^{n+1} \approx \Re\big\{\mathbf{G}_v^{(i)}\,\bar{\mathbf{V}}^n\big\}, \qquad \theta_i^{n+1} \approx \Re\big\{\mathbf{G}_\theta^{(i)}\,\boldsymbol{\Theta}^n\big\} \tag{87}$$

constitute the proposed Dirichlet-type absorbing boundary conditions for the LPS model. At each absorbing node, they prescribe displacement, velocity, and dilatation directly from local cloud data. The resulting update is entirely time-domain and requires neither spatial differential operators nor transform-based constructions, and it introduces no auxiliary evolution equations. Compared with the bond-based formulation in [19], the additional relation for θ_i^{n+1} is the essential structural extension required by ordinary state-based elasticity. The updating row $\mathbf{G}_\theta^{(i)}$ is derived from the same discrete-dispersion-consistent mode set and the same cloud collocation as $\mathbf{G}_u^{(i)}$ and $\mathbf{G}_v^{(i)}$. It introduces no new tunable parameters and ensures that the volumetric contribution in the absorbing layer, controlled by λ_{PD}, remains consistent with the outgoing far-field wave content across the considered wavenumber range and for general Poisson ratios. The present ABCs should be viewed as a genuinely new state-based absorbing formulation: the additional update is the mechanism that makes absorption compatible with ordinary state-based elastodynamics beyond the special bond-based limit.

Remark 1. The far-field representation assumes that, for each absorbing node $\mathbf{x}_i$, the associated cloud C_i is fully contained in the computational domain. Consequently, the collocation systems used to construct the updating operators are assembled from cloud data on a complete (untruncated) neighborhood, so that the moment matrices $\mathbf{A}_u$, $\mathbf{A}_v$, and $\mathbf{A}_\theta$ are free from surface-effect bias. The updating operators in (87) are computed independently for each absorbing node and applied locally; no additional smoothing or distribution of boundary values across the absorbing layer is required.

5. Implementation

The source code accompanying this work is publicly available at [33] and is released under the MIT licence. The repository contains the preprocessor and solver described below, together with build instructions, example inputs, and scripts to reproduce the numerical results of Section 6. The implementation is deliberately split into two stages. In an offline preprocessing stage, all quantities that depend only on the material parameters, discretization, and domain geometry are assembled once, including the discrete dispersion data, the cloud-wise least-squares systems, and the updating operators for the absorbing nodes. In the subsequent online solution stage, the transient peridynamic problem is advanced in time using these precomputed operators. As a result, the additional cost of the absorbing boundary conditions during time marching is minimal: at each absorbing node, the boundary update reduces to a small number of matrix–vector multiplications.

5.1. Preprocessing

The preprocessor takes as input the material parameters E, ν, ρ, the grid spacing Δx, the horizon δ, and the computational geometry, and writes binary data files that are read by the solver at startup. Its role is to convert the analytical construction of Sections 4.2 and 4.3 into discrete operators that can be reused throughout the simulation.

First, a fully interior template family is assembled in order to compute the discrete weighted volume m from (23). The same interior template is then used to evaluate the discrete quantities $\mathbf{S}$ and $\mathbf{N}$ in (53) and (54), and hence the dispersion matrix (55). This ensures that the outgoing basis used in the absorbing layer is calibrated against the same discrete quadrature and the same complete, untruncated horizon as the near-field solver. From the resulting value of m, the LPS coefficients κ and α follow from (16), and the volumetric coupling coefficient λ_{PD} is obtained from (34).

Next, the computational grid is generated, the absorbing set $\mathcal{A}$ is identified, and for each absorbing node $i\in\mathcal{A}$ its cloud C_i and local coordinate frame are constructed according to (56) and (57). Once the geometry of all clouds is known, the preprocessor evaluates candidate outgoing mode sets and assembles the corresponding least-squares systems. For a selected pair $(\Delta k,\Delta t)$, it constructs the mode basis over the prescribed angular window $\phi\in[-\Delta\phi,\Delta\phi]$, assembles the moment matrices (72) and (83), and computes the updating operators $\mathbf{G}_u^{(i)}$, $\mathbf{G}_v^{(i)}$, and $\mathbf{G}_\theta^{(i)}$ from (76) and (86) using an SVD-based least-squares solver (LAPACK `dgelsd`) with threshold $\varepsilon_{\mathrm{rcond}}$. The precise meaning

of the threshold $\varepsilon_{\mathrm{rcond}}$ (set to 10^{-14}) and its negligible effect on the operator construction and on stability are detailed in Appendix C.

This separation between offline construction and online application is important for efficiency. All expensive operations, including dispersion evaluation, basis assembly, and pseudoinverse computation, are performed only once. The solver therefore never recomputes modal information during time stepping; it only applies the stored cloud-wise operators.

5.2. Parameter selection

The practical performance of the proposed ABCs is governed primarily by two numerical parameters: the maximum sampled wavenumber Δk, which controls the spectral richness of the outgoing basis, and the time step Δt, which enters both the two-level temporal stencil and the target extrapolation from $\bar{t} = 0, -\Delta t$ to $\bar{t} = +\Delta t$. Their roles are complementary. Increasing Δk enriches the mode set and improves the ability of the absorbing layer to reproduce short-wavelength outgoing content, but it also increases the size of the least-squares system and may deteriorate its conditioning. Increasing Δt enlarges the temporal extrapolation interval and may likewise strengthen amplification in the update. In practice, the two parameters must therefore be selected together.

The angular aperture $\Delta\phi$ is treated separately. As discussed in Section 4.3, it defines a small outward-oriented window of admissible propagation directions and is fixed a priori to a value within the stability-admissible range determined from the non-amplification requirement of the updating operators (analyzed in Example 1, Section 6). The automatic calibration is then performed only over $(\Delta k, \Delta t)$. The candidate values are chosen within physically and numerically admissible ranges, namely

$$0 < \Delta k \le \frac{\pi}{\Delta x}, \qquad 0 < \Delta t \lesssim \frac{\Delta x}{c_{\mathrm{P}}},$$

where the first bound reflects discrete sampling and the second provides a conservative scale for explicit time integration.

To assess whether a candidate pair $(\Delta k, \Delta t)$ yields a nonamplifying absorbing update, we monitor the Frobenius norms of the displacement and velocity operators,

$$\max_i \max\left(\left\|\mathbf{G}_u^{(i)}\right\|_{\mathrm{F}}, \left\|\mathbf{G}_v^{(i)}\right\|_{\mathrm{F}}\right) \le 1. \tag{88}$$

The rationale for this criterion, and the precise sense in which bounding the Frobenius norm renders each boundary overwrite non-expansive in the ℓ^2 norm, are given in Appendix B; the screen is deliberately conservative, since $\|\mathbf{G}\|_2 \le \|\mathbf{G}\|_{\mathrm{F}}$. The screening is carried out only with $\mathbf{G}_u$ and $\mathbf{G}_v$, because these operators directly govern the displacement and velocity overwrite and are therefore the dominant quantities for boundary-driven stability. The dilatation operator $\mathbf{G}_\theta$ is left out of the screen because it overwrites an auxiliary field that is reconstructed at every step from the displacement rather than advanced in time, so its norm need not be bounded by unity for stability; in our examples $\max_i \|\mathbf{G}_\theta^{(i)}\|_{\mathrm{F}} \approx 1.1$, mildly above unity yet without effect on the long-time stability confirmed by the energy histories. Once an admissible pair has been identified, the corresponding dilatation operator $\mathbf{G}_\theta$ is assembled together with the final kinematic operators.

Rather than evaluating all absorbing nodes during the sweep, we use a representative subset $\mathcal{S} \subset \mathcal{A}$. This subset contains all geometrically most restrictive nodes, in particular nodes with reduced or asymmetric clouds such as corners, together with a fixed-size sample of the remaining absorbing nodes. For each candidate pair $(\Delta k_j, \Delta t_i)$ we compute

$$G_{\max}(\Delta k_j, \Delta t_i) = \max_{s\in\mathcal{S}} \max\left(\left\|\mathbf{G}_u^{(s)}\right\|_{\mathrm{F}}, \left\|\mathbf{G}_v^{(s)}\right\|_{\mathrm{F}}\right), \tag{89}$$

and select the admissible pair whose value is closest to unity,

$$(\Delta t^*, \Delta k^*) = \operatorname*{arg\,min}_{(i,j):\, G_{\max}(\Delta k_j, \Delta t_i)\le 1} G_{\max}(\Delta k_j, \Delta t_i). \tag{90}$$

This choice has a clear interpretation: among all candidate pairs that remain nonamplifying in the sense of (88), we retain the one that is least conservative. In this way, the mode set is made as expressive as possible without sacrificing stability of the absorbing update.

Algorithm 1 summarizes the complete preprocessing pipeline. It makes explicit that parameter selection is not an ad hoc tuning step performed after the operators are built; rather, it is integrated into the offline construction itself. The final operators stored for the solver are therefore already calibrated with respect to the discrete dispersion, the cloud geometry, and the stability screen.

This automatic calibration is itself a point of departure from the bond-based elastic ABCs [19]. There, the time step is fixed in advance from the explicit-integration limit, and the wavenumber sampling is selected by hand through a trial test on a single representative cloud, requiring only that the norm of the updating operators stay below unity, a condition adopted there by analogy with a fixed-point iteration. The present work uses the same non-amplification screen (88), now derived in Appendix B rather than assumed, but evaluates it automatically over the representative set $\mathcal{S}$. This automation is necessary because the volumetric coupling of the LPS model makes the admissible $(\Delta t, \Delta k)$ region depend on the Poisson ratio: a step size and sampling that are stable for one material need not be stable for another, so the time step and the wavenumber sampling are calibrated jointly and without user intervention rather than chosen by hand on a single cloud.

Algorithm 1: Offline calibration and construction of LPS absorbing boundary operators

Data: candidate sets $\{\Delta k_j\}$ and $\{\Delta t_i\}$; fixed angular window $\Delta\phi$; absorbing set $\mathcal{A}$ with clouds C_i and local angles τ_i; representative subset $\mathcal{S} \subset \mathcal{A}$; SVD threshold $\varepsilon_{\mathrm{rcond}}$
Result: selected parameters $(\Delta t^*, \Delta k^*)$ and cloud-wise operators $\mathbf{G}_u^{(i)}, \mathbf{G}_v^{(i)}, \mathbf{G}_\theta^{(i)}$ for all $i \in \mathcal{A}$

assemble a fully interior template family and compute m from (23);
compute κ, α, and λ_{PD} from (16) and (34);
evaluate the discrete dispersion ingredients $\mathbf{S}$, $\mathbf{N}$, and $\mathbf{M}^{\mathrm{LPS}}$ from (53)–(55);
generate the computational grid, identify $\mathcal{A}$, and assemble the clouds C_i and local frames τ_i;
foreach Δk_j **do**
  construct the outgoing mode set with $k \in (0, \Delta k_j]$ and $\phi \in [-\Delta\phi, \Delta\phi]$;
  compute the associated mode data from (47);
  foreach Δt_i **do**
    $G_{\max} \leftarrow 0$;
    foreach $s \in \mathcal{S}$ **do**
      assemble $\mathbf{A}_u$ and $\mathbf{A}_v$ from (72) at $\bar{t} = 0, -\Delta t_i$;
      compute $\mathbf{G}_u^{(s)}$ and $\mathbf{G}_v^{(s)}$ from (76) using SVD least squares;
      update $G_{\max} \leftarrow \max\left(G_{\max}, \|\mathbf{G}_u^{(s)}\|_{\mathrm{F}}, \|\mathbf{G}_v^{(s)}\|_{\mathrm{F}}\right)$;
    store $G_{\max}(\Delta k_j, \Delta t_i)$;
select the optimal pair $(\Delta t^*, \Delta k^*)$ automatically according to (90);
rebuild the outgoing mode set using Δk^* and Δt^*;
foreach $i \in \mathcal{A}$ **do**
  assemble $\mathbf{A}_u$, $\mathbf{A}_v$, and $\mathbf{A}_\theta$ from (72) and (83) at $\bar{t} = 0, -\Delta t^*$;
  compute $\mathbf{G}_u^{(i)}$, $\mathbf{G}_v^{(i)}$, and $\mathbf{G}_\theta^{(i)}$ from (76) and (86) using SVD least squares;
  store the operators together with the cloud index list for node i;

5.3. Time stepping with absorbing boundary conditions

At run time, the solver reads the precomputed clouds, mode data, and updating operators, and advances the peridynamic system by the velocity Verlet scheme (28)–(29) augmented by the absorbing updates (87). The resulting algorithm is explicit and differs from the standard LPS time integrator only through the local overwrite operations applied at the absorbing nodes.

The order of operations is dictated by the structure of the LPS model. Because the internal forces depend on the dilatation through the volumetric contribution in (32) and (35), each time step begins with the predictor

$$\mathbf{u}_i^{n+1} = \mathbf{u}_i^n + \Delta t\, \dot{\mathbf{u}}_i^n + \frac{\Delta t^2}{2}\, \ddot{\mathbf{u}}_i^n,$$

after which a provisional dilatation field is computed from (23). For interior nodes this quadrature-based value is used directly. For absorbing nodes, however, truncated horizons bias the quadrature-based dilatation; therefore, the provisional value is replaced by the precomputed far-field update

$$\theta_i^{n+1} = \mathfrak{R}\big\{\mathbf{G}_\theta^{(i)}\, \boldsymbol{\Theta}^n\big\}, \qquad i \in \mathcal{A},$$

before the force assembly is performed. With the corrected dilatation field available, the solver evaluates the internal forces and hence the accelerations $\ddot{\mathbf{u}}^{n+1}$ from (24). The displacement and velocity are then advanced by velocity Verlet, and finally the absorbing node values are overwritten using the precomputed kinematic updates

$$\mathbf{u}_i^{n+1} = \mathfrak{R}\big\{\mathbf{G}_u^{(i)}\, \bar{\mathbf{U}}^n\big\}, \qquad \dot{\mathbf{u}}_i^{n+1} = \mathfrak{R}\big\{\mathbf{G}_v^{(i)}\, \bar{\mathbf{V}}^n\big\}, \qquad i \in \mathcal{A}.$$

This procedure highlights the main implementation advantage of the proposed ABCs: all nontrivial boundary modeling is embedded in precomputed linear operators. No auxiliary evolution equations, no transform evaluations, and no additional local solves are required during time stepping. Consequently, once the offline calibration has been completed, the absorbing treatment adds only a modest overhead to a standard explicit LPS solver, as quantified for the benchmark domain in Example 1 (Fig. 9). The full update is summarized in Algorithm 2.

Algorithm 2: Velocity Verlet time step with LPS absorbing boundary conditions

Data: fields $(\mathbf{u}^n, \dot{\mathbf{u}}^n, \ddot{\mathbf{u}}^n)$ with histories $(\mathbf{u}^{n-1}, \dot{\mathbf{u}}^{n-1})$; dilatation history (θ^n, θ^{n-1}); absorbing set $\mathcal{A}$; operators $\mathbf{G}_u^{(i)}, \mathbf{G}_v^{(i)}, \mathbf{G}_\theta^{(i)}$
Result: $(\mathbf{u}^{n+1}, \dot{\mathbf{u}}^{n+1}, \ddot{\mathbf{u}}^{n+1})$ and θ^{n+1}

foreach *node* i **do**
  $\mathbf{u}_i^{n+1} \leftarrow \mathbf{u}_i^n + \Delta t\, \dot{\mathbf{u}}_i^n + \frac{\Delta t^2}{2}\, \ddot{\mathbf{u}}_i^n$; // (28)
compute provisional θ^{n+1} from $\mathbf{u}^{n+1}$ using (23);
foreach $i \in \mathcal{A}$ **do**
  $\theta_i^{n+1} \leftarrow \mathfrak{R}\{\mathbf{G}_\theta^{(i)}\, \boldsymbol{\Theta}^n\}$; // (85)
compute $\ddot{\mathbf{u}}^{n+1}$ from (24);
foreach $i \in \mathcal{A}$ **do**
  $\mathbf{u}_i^{n+1} \leftarrow \mathfrak{R}\{\mathbf{G}_u^{(i)}\, \bar{\mathbf{U}}^n\}$; // (74)
foreach *node* i **do**
  $\dot{\mathbf{u}}_i^{n+1} \leftarrow \dot{\mathbf{u}}_i^n + \frac{\Delta t}{2}\big(\ddot{\mathbf{u}}_i^n + \ddot{\mathbf{u}}_i^{n+1}\big)$; // (29)
foreach $i \in \mathcal{A}$ **do**
  $\dot{\mathbf{u}}_i^{n+1} \leftarrow \mathfrak{R}\{\mathbf{G}_v^{(i)}\, \bar{\mathbf{V}}^n\}$; // (75)
$(\mathbf{u}^{n-1}, \dot{\mathbf{u}}^{n-1}, \theta^{n-1}) \leftarrow (\mathbf{u}^n, \dot{\mathbf{u}}^n, \theta^n)$;
$(\mathbf{u}^n, \dot{\mathbf{u}}^n, \theta^n) \leftarrow (\mathbf{u}^{n+1}, \dot{\mathbf{u}}^{n+1}, \theta^{n+1})$;

6. Numerical tests

In this section, the numerical performance of the proposed ABCs is assessed on two benchmark problems in two-dimensional unbounded domains. The first (Example 1) is a radially symmetric Gaussian pulse, on which we also establish the stability-admissible angular aperture and its independence of the material; the second (Example 2) places an internal baffle in the domain, so that the pulse is diffracted and the absorbing boundary is struck by a complex, multi-directional wave field. The material properties are chosen similar to those of steel 18Ni1900, with Young's modulus $E = 190 \times 10^3\,\mathrm{N/mm^2}$, density $\rho = 8000 \times 10^{-9}\,\mathrm{kg/mm^3}$, and three Poisson ratios $\nu \in \{0.15, 0.30, 0.45\}$, so that the influence of the Poisson ratio on the absorption quality can be studied systematically. All computations assume plane strain conditions. The peridynamic horizon is $\delta = 2\,\mathrm{mm}$ with a uniform grid spacing $\Delta x = 0.5\,\mathrm{mm}$ (horizon ratio $\delta/\Delta x = 4$). Time integration is performed by the velocity Verlet scheme of Section 5.3 with time step $\Delta t = 35 \times 10^{-3}\,\mu\mathrm{s}$.

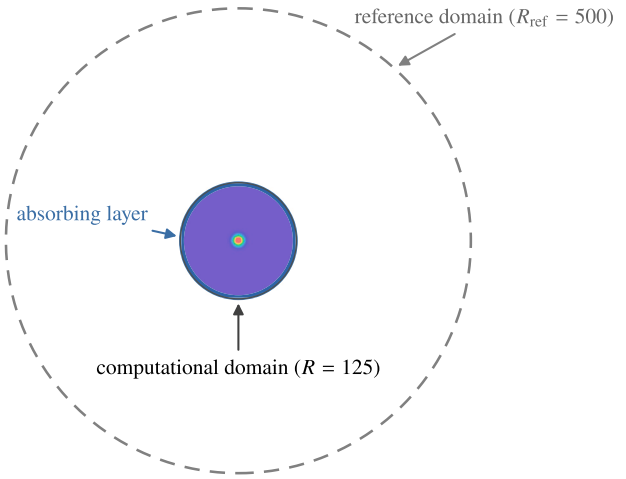

Fig. 7. Setup of Example 1, shown to scale: the truncated computational domain ($R = 125\,\mathrm{mm}$) with its absorbing layer, centered within the large free-boundary reference domain ($R_{\mathrm{ref}} = 500\,\mathrm{mm}$). The color field is the initial Gaussian displacement pulse.

The computational (truncated) domain is a circular region of radius $R = 125\,\mathrm{mm}$. The absorbing boundary Γ_∞ coincides with the outer circle, and the absorbing layer $\mathcal{A}$ collects all nodes within one horizon of Γ_∞ (see the setup in Fig. 7). For the reference solution, the same problem is solved on a large circular domain of radius $R_{\mathrm{ref}} = 500\,\mathrm{mm}$ with traction-free (homogeneous Neumann) boundary conditions; the simulation is terminated before waves reach the outer boundary of this extended domain, so that the reference solution is free from boundary effects. Contour plots report the truncated-domain and reference-domain results restricted to the same inner region, together with their pointwise difference. We note that, although a circular truncated domain is used here, the proposed approach is equally applicable to rectangular or other convex domain shapes, as demonstrated for bond-based peridynamics in [20]; rectangular domains are omitted here for brevity.

6.1. Example 1: radially symmetric pulse

The source of excitation is an initial displacement field in the form of a truncated Gaussian pulse centered at the origin,

$$\mathbf{u}^0(r,\vartheta) = \begin{cases} \exp\!\big(-\frac{1}{100}\, r^2\big)\,(\cos\vartheta, \sin\vartheta)^{\mathrm{T}}, & 0 < r \le 40, \\ \mathbf{0}, & \text{otherwise}, \end{cases} \qquad \dot{\mathbf{u}}^0 = \mathbf{0}, \tag{91}$$

where r and ϑ are polar coordinates. This purely radial pulse excites both P- and S-wave content and produces a dispersive wave field that reaches the absorbing boundary at different times depending on the Poisson ratio.

The online time stepping was performed on the same machine using OpenMP parallelization. The absorbing boundary parameters were selected automatically by the preprocessing sweep of Algorithm 1.

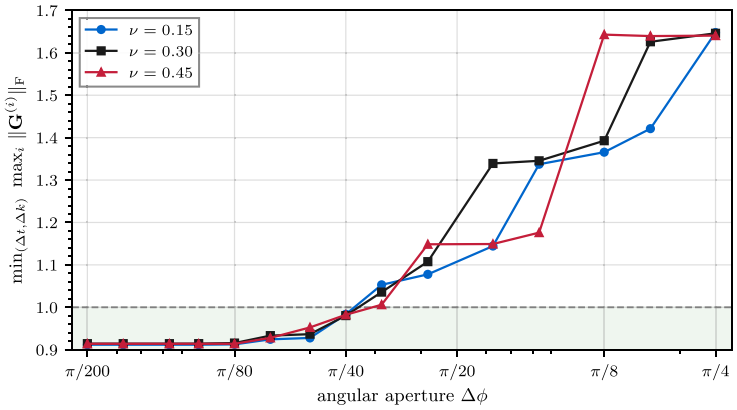

Fig. 8. Stability-admissible angular aperture for Example 1. The quantity $g_{\min}(\Delta\phi) = \min_{(\Delta t,\Delta k)} \max_i \|\mathbf{G}^{(i)}\|_F$ is a property of the absorbing operators alone; it remains below the non-amplification limit (dashed) up to $\Delta\phi \approx \pi/40$ and exceeds it beyond, essentially independently of the Poisson ratio.

We use Example 1 to put the choice of the angular aperture $\Delta\phi$ on a rigorous footing. The admissible aperture is governed by the non-amplification criterion (88): for each candidate $\Delta\phi$ we evaluate $g_{\min}(\Delta\phi) = \min_{(\Delta t,\Delta k)} \max_i \|\mathbf{G}^{(i)}\|_F$, the smallest operator norm attainable over the calibration of the time step and wavenumber sampling, on the geometrically most restrictive clouds. This quantity is a property of the absorbing operators alone, independent of the source, the initial condition, or the wave field, and therefore bounds the aperture for any problem discretized at the same resolution. Fig. 8 shows $g_{\min}(\Delta\phi)$ for the three Poisson ratios. The curves are essentially indistinguishable in the stable regime and cross unity at the same aperture, $\Delta\phi \approx \pi/40$: below this value a non-amplifying operator exists, while above it none does at any admissible time step. The admissible aperture is thus essentially material-independent, and the value used in all computations reported here lies comfortably within it. We note that, within the stable range, the largest admissible time step remains at the explicit-integration limit irrespective of $\Delta\phi$; increasing the aperture is accommodated by reducing the wavenumber sampling Δk rather than by altering Δt.

We also quantify the computational overhead of the proposed treatment on the present benchmark. Fig. 9 reports the cost of the offline operator construction. Because the updating operators are built independently for each absorbing node, the total construction time scales linearly with the number of absorbing nodes N (Fig. 9a), and the per-node work is independent across nodes and parallelizes efficiently: on a 16-core workstation the construction reaches a speedup of about 11.7 (Fig. 9b). The per-node cost grows with the horizon ratio $\delta/\Delta x$ (Fig. 9c), since the size of the cloud, and hence of the local least-squares system solved for each node, increases as $N_c \sim (\delta/\Delta x)^2$. For the discretization used here ($\delta/\Delta x = 4$), constructing all operators for the $N = 6268$ absorbing nodes of the $R = 125\,\mathrm{mm}$ domain takes about 2.5 s on eight cores, comparable to the cost of only about 224 explicit time steps; since a typical simulation runs several thousand steps, the one-time construction amounts to a few percent of the online cost.

The online overhead is similarly modest. The absorbing nodes form a thin boundary layer, here about 3% of the $N_{\mathrm{total}} = 196,321$ domain nodes, and each is advanced by a fixed, small number of precomputed matrix–vector products; the overhead therefore does not grow with the interior and becomes asymptotically negligible under mesh refinement, the boundary scaling only as $\mathcal{O}(\sqrt{N_{\mathrm{total}}})$. On structured portions of the boundary the saving is larger still: absorbing nodes that share the same outward normal and the same cloud arrangement, such as those along a flat boundary segment, have identical updating operators that can be built once and reused. Finally, this overhead should be weighed against the alternative of suppressing reflections by enlarging the domain so that waves do not return within the simulation time, which would inflate both the preprocessing and every online step over the entire extended mesh; the absorbing treatment avoids that cost altogether.

Figs. 10–12 show contour plots of displacement magnitude $\|\mathbf{u}\|$, velocity magnitude $\|\dot{\mathbf{u}}\|$, and dilatation magnitude $|\theta|$ at four representative time instants for $\nu = 0.30$. In each figure, the left column displays the truncated-domain solution obtained with the proposed ABCs, the middle column shows the reference solution restricted to the same region, and the right column reports the pointwise difference. At early times, the truncated and reference solutions are in close agreement; as the wave front crosses Γ_∞, the absorbing layer transmits the outgoing content with minimal reflection, and the difference fields remain small throughout the simulation. The simultaneous agreement in displacement, velocity, and especially dilatation is a strong indicator that the proposed state-based ABCs are capturing the full LPS wave structure rather than only its kinematic part.

The energy evolution within the computational domain is reported in Figs. 13–15 for all three Poisson ratios. In each case, the total energy of the truncated-domain solution decreases monotonically once the wave front reaches the boundary, closely following the reference trend. This confirms that the proposed ABCs absorb the outgoing energy without introducing significant reflections. The detailed shape of this decay is itself Poisson-ratio dependent. The energy leaves the computational domain as the compressional and shear wave packets successively cross the absorbing boundary, at times set by their group velocities. The peridynamic speeds are dispersive, so no single speed ratio applies; in the long-wavelength limit, however, where the LPS model recovers classical elasticity, the ratio is $c_P/c_S = \sqrt{2(1-\nu)/(1-2\nu)}$, rising from about 1.6 at $\nu = 0.15$ to about 3.3 at $\nu = 0.45$. Since the smooth Gaussian pulse is dominated by long-wavelength content (small $k\delta$), where the discrete dispersion stays close to this limit (Fig. 4), this ratio governs the leading separation of the two packets. As ν increases they therefore reach the boundary at increasingly separated times: at $\nu = 0.45$ the wide separation produces a more pronounced, stepped decay with distinct compressional and shear stages, whereas at $\nu = 0.15$ the nearly coincident arrivals give a smoother curve. The residual dispersion of the shorter-wavelength content (Fig. 4) modifies the detailed shape but not this trend. To verify long-term stability, the truncated-domain simulation with ABCs was continued well beyond the time at which all wave content has left the computational domain. No growth of energy or onset of instability is observed, as is evident from the energy plots, demonstrating that the proposed absorbing boundary treatment remains stable over extended simulation times. Taken together, these results support the claim that the present method solves a harder problem than the earlier bond-based ABCs [19] while retaining strong absorption and stable time integration.

6.2. Example 2: diffracted wave field with an internal baffle

To assess the absorbing boundary conditions on a more demanding wave field, we repeat the test of Example 1 with an internal baffle

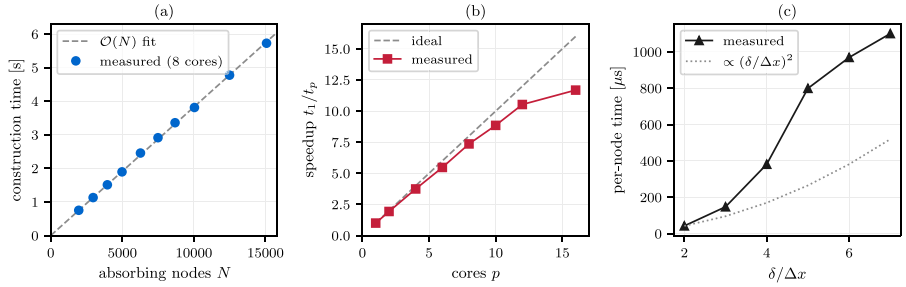

Fig. 9. Cost of the offline construction of the absorbing updating operators. (a) Total construction time versus the number of absorbing nodes N (circular domains of increasing radius, $\delta/\Delta x = 4$): the cost scales linearly, $\mathcal{O}(N)$. (b) Parallel speedup t_1/t_p versus the number of cores p (here $N = 12\,492$), where t_p denotes the construction wall-clock time on p cores (so t_1 is the single-core time): the per-node build is independent across nodes and parallelizes efficiently, reaching about 11.7× on 16 cores. (c) Per-node construction time versus the horizon ratio $\delta/\Delta x$. The cloud size, which sets the row dimension of the per-node least-squares system, grows as $N_c \sim (\delta/\Delta x)^2$ (dotted reference); the per-node time grows somewhat faster still, reflecting the superlinear cost of the dense least-squares solve.

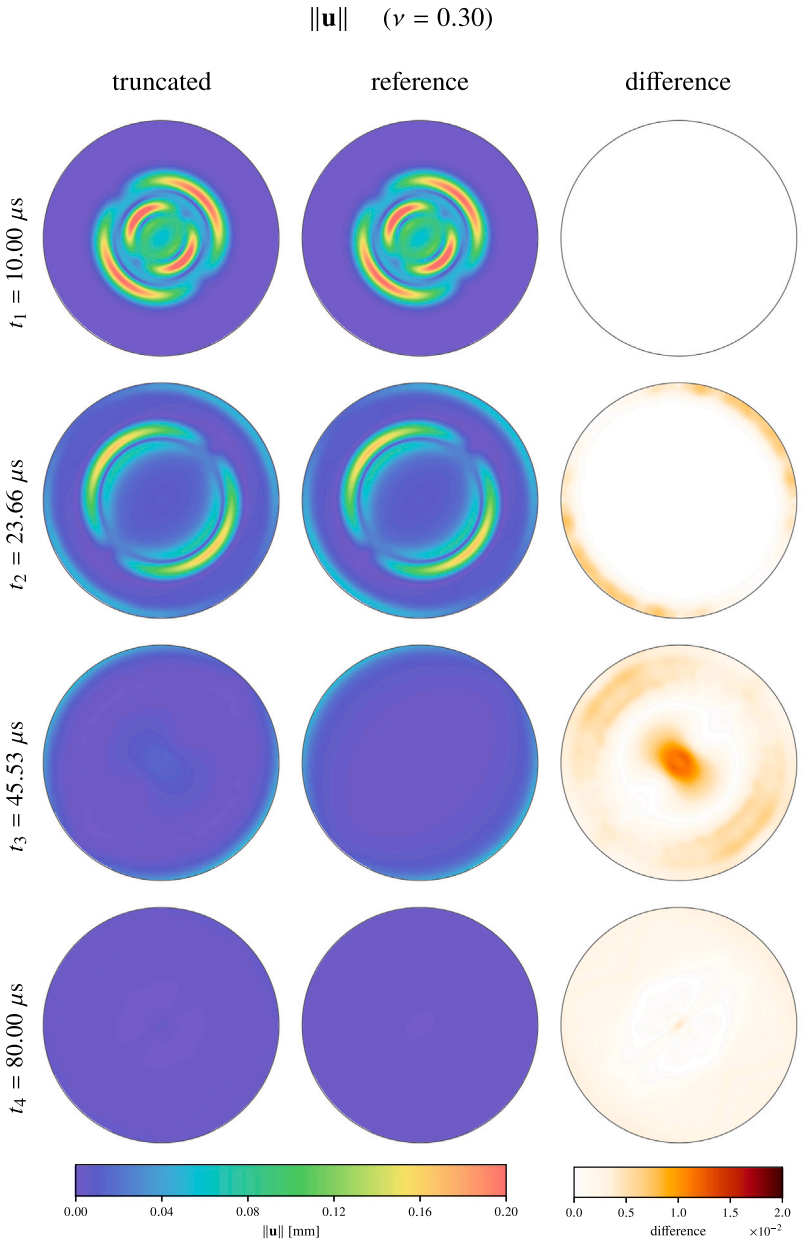

Fig. 10. Contour plots of displacement magnitude $\|\mathbf{u}\|$ obtained for the Gaussian pulse propagation at four time instants within the computational domain for $\nu = 0.30$. Left column: truncated domain with the proposed ABCs; middle column: reference solution (large domain with free boundaries); right column: pointwise difference between truncated and reference solutions.

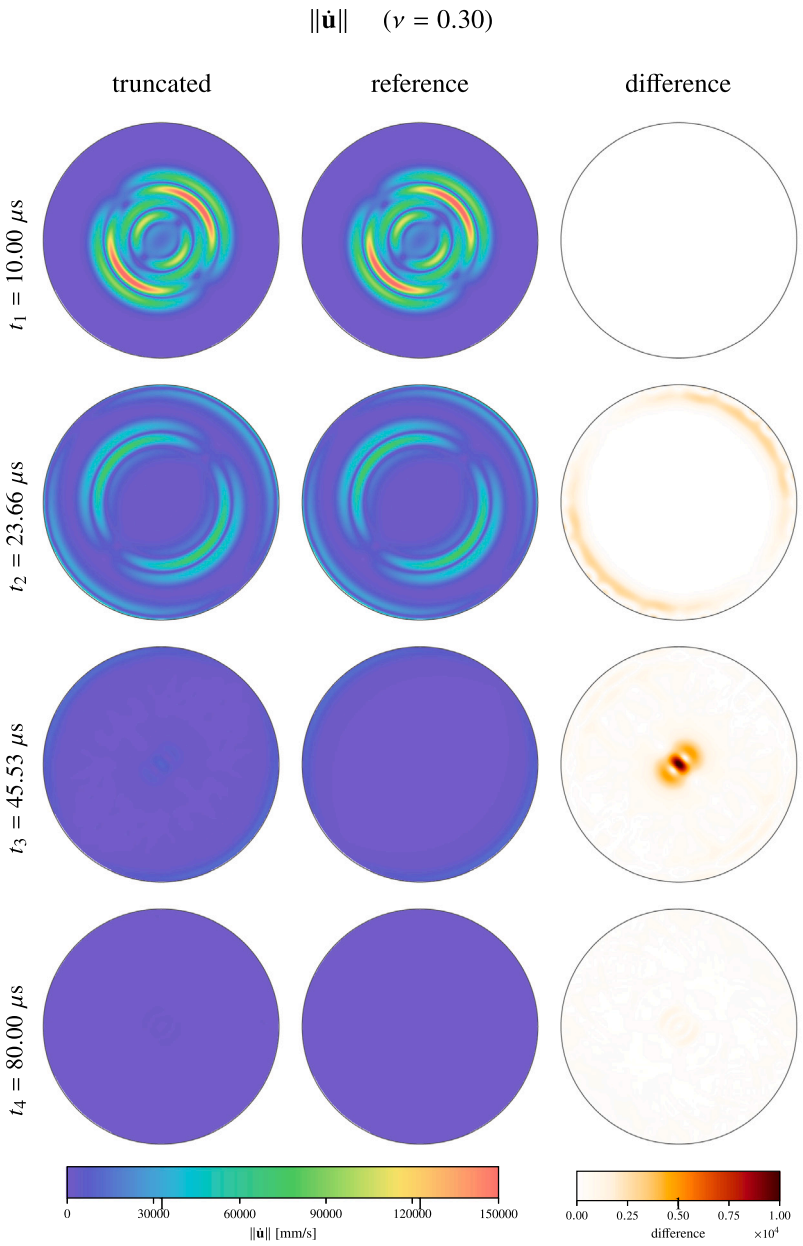

Fig. 11. Contour plots of velocity magnitude $\|\dot{\mathbf{u}}\|$ obtained at the same time instants and for the same configuration as in Fig. 10 ($\nu = 0.30$). Columns are arranged as in Fig. 10.

placed in the computational domain. The baffle is a horizontal segment of length 60 mm centered at $(0, 30\,\text{mm})$ (Fig. 16); all bonds crossing it are removed, so that it acts as a traction-free internal crack. The material parameters, discretization, truncated and reference domains, and the initial Gaussian pulse are identical to those of Example 1. As the pulse expands it is diffracted around the tips of the baffle, producing a complex field that reaches the absorbing boundary over a broad and continuously varying range of incidence directions, rather than near-normally as in the radially symmetric Example 1. This provides a stringent, multi-directional test of the absorbing treatment, which we carry out for all three Poisson ratios.

Fig. 17 shows the displacement magnitude in the truncated and reference domains, together with their pointwise difference, at comparable instants for the three Poisson ratios. Despite the complexity of the diffracted field, the truncated-domain solution is visually indistinguishable from the reference, and the difference fields remain negligible across all materials. The energy histories confirm this quantitatively. Fig. 18 reports the difference between the near-field energy of the truncated and reference solutions, normalized by the initial energy E_0. The spurious energy remains of the order of 0.1 % of E_0 for $\nu = 0.15$ and $\nu = 0.30$ and reaches about 1.3 % for $\nu = 0.45$, the slightly larger residual at the highest Poisson ratio being consistent with the stronger volumetric coupling of the LPS model. Since an arbitrary outgoing field can be regarded as a superposition of plane-wave modes, the low reflection of a strongly diffracted, multi-directional field provides direct evidence that the proposed ABCs perform well in the general case, across the range of materials considered. This normalized energy difference, evaluated over the near-field region and the time window in which the reference is free of boundary effects, is a global and quantitative measure of the spurious energy retained by the truncation, and thus serves as a quantitative reflection-error indicator. We favor it over a single reflection coefficient because, in the present dispersive medium, the phase velocity varies with wavenumber (Fig. 4) and the field reaches the boundary over a continuous range of directions, so that

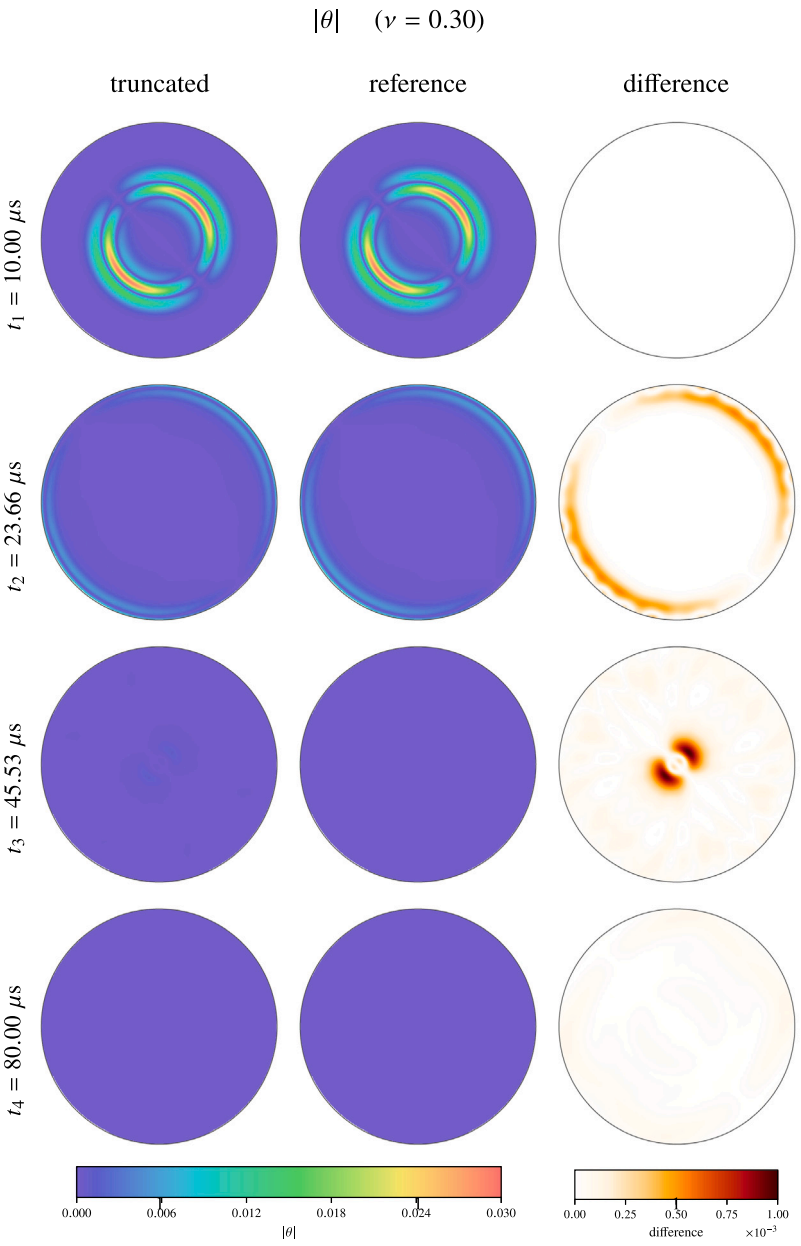

Fig. 12. Contour plots of dilatation magnitude $|\theta|$ obtained at the same time instants and for the same configuration as in Fig. 10 ($\nu = 0.30$). Columns are arranged as in Fig. 10.

a scalar coefficient would depend on the chosen frequency, incidence angle, and wave mode; the energy measure instead aggregates the entire outgoing content into one well-defined quantity. Complementing it, the pointwise difference fields in the right-hand columns of the contour plots (Figs. 10–12 for Example 1 and Fig. 17 for Example 2) provide a full-field comparison with the reference at several instants.

7. Conclusions

We have presented time-domain, Dirichlet-type absorbing boundary conditions for two-dimensional ordinary state-based peridynamic elastodynamics within the Linear Peridynamic Solid (LPS) framework. Outgoing waves are represented by plane-wave modes that satisfy the discrete LPS dispersion relation, and a cloud-based collocation and least-squares procedure converts this representation into precomputable operators that prescribe displacement, velocity, and dilatation directly at the absorbing nodes during explicit time stepping. The construction is distinguished by three features: it resolves the coupled compressional and shear branches together with their Poisson-ratio dependence at the level of the numerical discretization; it advances the nonlocal dilatation consistently at truncated horizons through a dedicated updating operator, which removes the need for surface-correction procedures in the absorbing layer; and it calibrates the sampling parameters automatically through a Frobenius-norm non-amplification screen. Numerical experiments across a range of Poisson ratios, including a strongly diffracted, multi-directional field, confirm that the resulting ABCs suppress spurious reflections to at most about one percent of the initial energy and remain stable over long simulations, at a cost of only a few matrix–vector products per absorbing node per step. The method is therefore well suited to unbounded elastodynamic problems in meshfree state-based peridynamics with arbitrary Poisson ratio, and it integrates into existing explicit solvers through the publicly

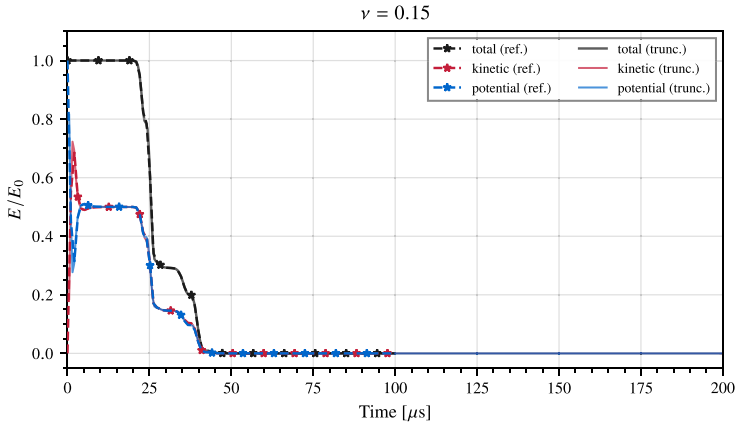

Fig. 13. Variation of kinetic, potential, and total energy within the computational domain for $\nu = 0.15$. Solid lines: truncated domain with the proposed ABCs; dashed lines with markers: reference domain.

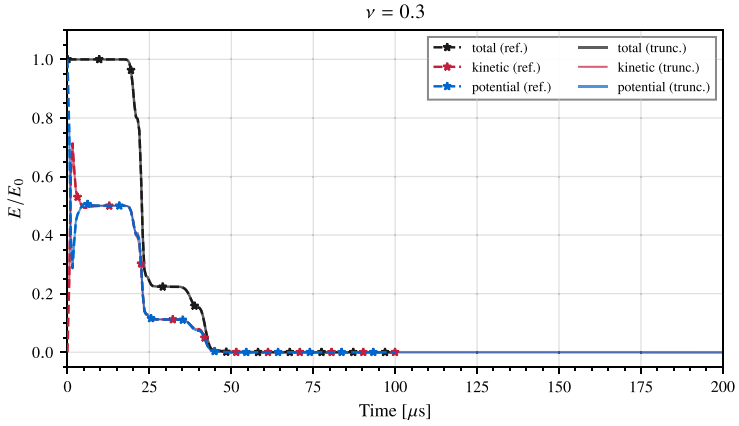

Fig. 14. Variation of kinetic, potential, and total energy within the computational domain for $\nu = 0.30$. Solid lines: truncated domain with the proposed ABCs; dashed lines with markers: reference domain.

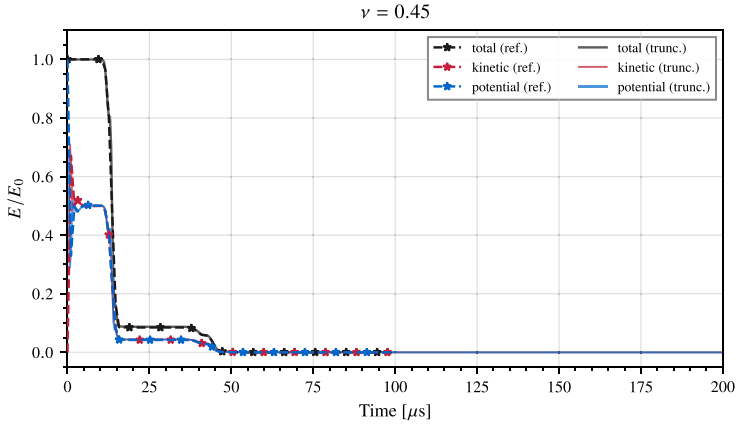

Fig. 15. Variation of kinetic, potential, and total energy within the computational domain for $\nu = 0.45$. Solid lines: truncated domain with the proposed ABCs; dashed lines with markers: reference domain.

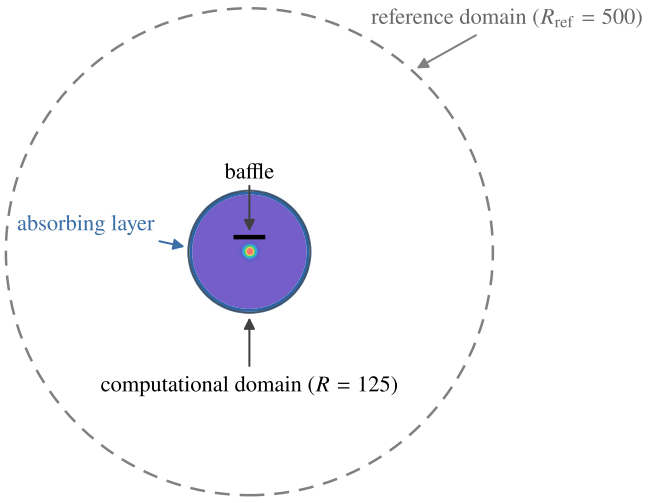

Fig. 16. Setup of Example 2: the configuration of Fig. 7 with an internal baffle (a 60 mm traction-free segment centered at (0, 30 mm)) that diffracts the outgoing pulse.

available implementation. Its present scope is also its main limitation: the absorbing layer assumes a linear, undamaged far field, the formulation and examples are restricted to two dimensions under plane strain, and the residual reflection grows mildly towards the incompressible limit. Natural extensions are to three dimensions, to anisotropic and to nonlinear or damaged near-field regions, and to other state-based constitutive models, for which the discrete-dispersion-consistent modal construction developed here provides a direct template.

CRediT authorship contribution statement

Alexander Hermann: Writing – review & editing, Writing – original draft, Validation, Software, Methodology, Investigation, Formal analysis, Conceptualization. **Arman Shojaei:** Writing – review & editing, Writing – original draft, Visualization, Methodology, Investigation, Formal analysis, Conceptualization. **Christian J. Cyron:** Writing – review & editing, Supervision, Resources, Funding acquisition.

Declaration of Generative AI and AI-assisted technologies in the writing process

During the preparation of this work the Authors used OpenAI ChatGPT in order to improve language and readability of the text. After using this service, the Authors reviewed and edited the content as needed and take full responsibility for the content of the publication.

Declaration of competing interest

The authors declare that they have no known competing financial interests or personal relationships that could have appeared to influence the work reported in this paper.

Acknowledgments

Funded by the Deutsche Forschungsgemeinschaft (DFG, German Research Foundation) as part of the Excellence Strategy of the Federal Government and the federal states – EXC 3120/1 – 533771286.

Appendix A. Classical limit of the LPS dispersion relation

In the long-wavelength limit $k\delta \to 0$ (vanishing nonlocality), the LPS dispersion relation recovers the classical plane-strain elastic relations. This follows by Taylor expanding the kernels in (40) and (44) for $|\bar{\boldsymbol{\alpha}} \cdot \boldsymbol{\xi}| \ll 1$, where $k = \|\bar{\boldsymbol{\alpha}}\|$ and $\hat{\alpha}_j = \bar{\alpha}_j/k$. The sine-integral vector satisfies

$$S_l(\bar{\boldsymbol{\alpha}}) = \mathrm{i}\,\frac{m}{d}\,\bar{\alpha}_l + \mathcal{O}\big((k\delta)^3\big), \qquad k\delta \to 0, \tag{A.1}$$

while the deviatoric matrix has the leading-order form

$$N_{jl}(\bar{\boldsymbol{\alpha}}) = -\frac{m}{2d(d+2)}\Big(k^2\delta_{jl} + 2\bar{\alpha}_j\bar{\alpha}_l\Big) + \mathcal{O}\big((k\delta)^4\big), \qquad k\delta \to 0, \tag{A.2}$$

with δ_{jl} the Kronecker delta. Substituting (A.1) and (A.2) into (48) and using (15) and (16) yields

$$\lim_{k\delta\to 0} \mathbf{M}^{\mathrm{LPS}}(\bar{\boldsymbol{\alpha}}) = -\Big(\mu\,k^2\mathbf{I} + (\lambda+\mu)\,\bar{\boldsymbol{\alpha}}\,\bar{\boldsymbol{\alpha}}^{\mathrm{T}}\Big), \tag{A.3}$$

which is the plane-strain Christoffel matrix of isotropic linear elasticity. Consequently,

$$\lim_{k\delta\to 0}\frac{\bar{\omega}_{\mathrm{P}}}{k} = c_{\mathrm{P}}, \qquad \lim_{k\delta\to 0}\frac{\bar{\omega}_{\mathrm{S}}}{k} = c_{\mathrm{S}}. \tag{A.4}$$

Appendix B. Non-amplification screen for the updating operators

The rationale for the criterion (88) is as follows. Each absorbing update (74)–(75) reconstructs the boundary kinematics at t^{n+1} from the stored cloud history through a linear map, and we require this reconstruction to be non-expansive in the discrete Euclidean (ℓ^2) norm, so that the overwrite cannot inflate the boundary amplitude relative to the interior data that feed it. This requirement is motivated by the power-boundedness of a stationary linear iteration $\mathbf{w}^{n+1} = \mathbf{G}\,\mathbf{w}^n$, for which $\|\mathbf{G}\| \le 1$ in any submultiplicative norm yields $\|\mathbf{w}^n\| \le \|\mathbf{w}^0\|$ for all n [34, §5.6]. We stress that this is a guiding analogy rather than a direct application: the reconstruction operator $\mathbf{G}^{(i)}$ is rectangular ($2\times 4N_c$) and is not iterated on its own output, so the power-boundedness result does not apply to it as such; it serves only to justify imposing a per-overwrite non-amplification screen.

The Frobenius norm furnishes such a screen and is, in addition, inexpensive to evaluate. It is consistent with the Euclidean vector norm: for any matrix $\mathbf{G}$ with rows $\mathbf{g}_r$ and any vector $\mathbf{w}$, the Cauchy–Schwarz inequality gives

$$\|\mathbf{G}\mathbf{w}\|_2^2 = \sum_r \big|\mathbf{g}_r \cdot \mathbf{w}\big|^2 \le \Big(\sum_r \|\mathbf{g}_r\|_2^2\Big)\|\mathbf{w}\|_2^2 = \|\mathbf{G}\|_{\mathrm{F}}^2\,\|\mathbf{w}\|_2^2,$$

so that $\|\mathbf{G}\mathbf{w}\|_2 \le \|\mathbf{G}\|_{\mathrm{F}}\|\mathbf{w}\|_2$ and hence $\|\mathbf{G}\|_2 \le \|\mathbf{G}\|_{\mathrm{F}}$ [35]. Since taking the real part is also non-expansive, $\|\Re\{\mathbf{z}\}\|_2 \le \|\mathbf{z}\|_2$, imposing (88) makes each overwrite individually non-expansive,

$$\|\mathbf{u}_i^{n+1}\|_2 \le \|\mathbf{G}_u^{(i)}\|_{\mathrm{F}}\,\|\bar{\mathbf{U}}^n\|_2 \le \|\bar{\mathbf{U}}^n\|_2, \qquad \|\dot{\mathbf{u}}_i^{n+1}\|_2 \le \|\mathbf{G}_v^{(i)}\|_{\mathrm{F}}\,\|\bar{\mathbf{V}}^n\|_2 \le \|\bar{\mathbf{V}}^n\|_2,$$

so that the reconstructed boundary value can never exceed, in the ℓ^2 sense, the cloud data from which it is built.

The criterion is thus a local, one-step sufficient condition for the non-expansiveness of each reconstruction, and it is deliberately conservative. Because $\|\mathbf{G}\|_2 \le \|\mathbf{G}\|_{\mathrm{F}}$, bounding the Frobenius norm is stricter than bounding the operator 2-norm, and the $\Re\{\cdot\}$ projection of the complex operator onto the real cloud data can only reduce, never increase, the effective gain. We accept this conservatism in exchange for a screen that is read directly from the entries of $\mathbf{G}^{(i)}$ without any eigenvalue or singular-value computation, which is essential because the criterion is evaluated for every candidate pair $(\Delta k, \Delta t)$ on the most restrictive clouds during the offline sweep. We do not claim that this per-node bound by itself guarantees power-boundedness of the fully coupled interior-integration and overlapping-cloud overwrite operator; global stability over long simulations is confirmed separately by the energy histories reported in Section 6, which exhibit no growth once the wave field has left the domain. The same non-amplification

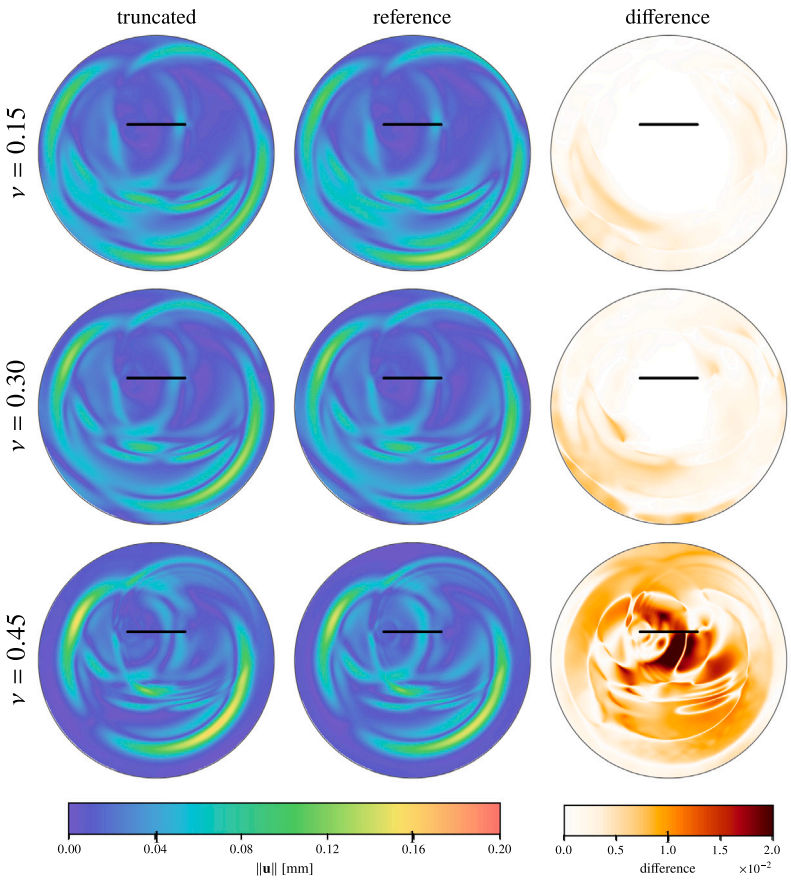

Fig. 17. Example 2: displacement magnitude $\|\mathbf{u}\|$ of the truncated-domain solution with the proposed ABCs (left), the reference solution restricted to the same region (middle), and their pointwise difference (right), at $t \approx 34\,\mu s$ (for $\nu = 0.45$, $t \approx 32\,\mu s$), when the diffracted field interacts with the absorbing boundary, for the three Poisson ratios. The black segment marks the baffle. The agreement is maintained throughout the simulation; see the energy comparison in Fig. 18.

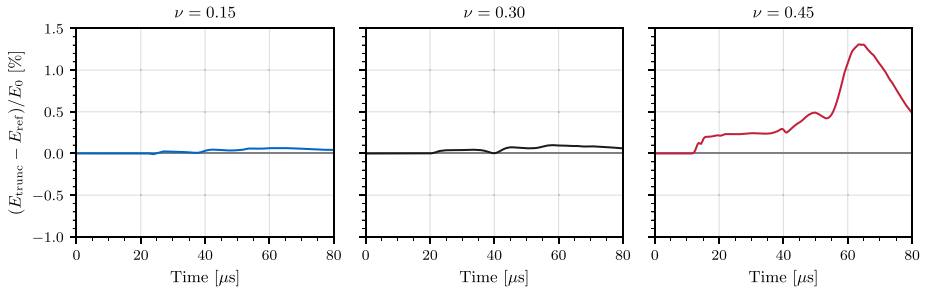

Fig. 18. Example 2: difference between the near-field energy of the truncated-domain (ABC) and reference solutions, normalized by the initial energy E_0, for the three Poisson ratios. The spurious reflected energy remains of the order of 0.1 % of E_0 for $\nu = 0.15$ and $\nu = 0.30$ and reaches about 1.3 % for $\nu = 0.45$.

screen underlies the bond-based construction [19], where the norm of the updating operators was likewise required to stay below unity; there, however, it was adopted by analogy with a fixed-point iteration, whereas the derivation above supplies the justification that was previously absent.

Appendix C. Truncated-SVD regularization of the moment matrices

The updating operators are obtained from the moment matrices (72) and (83) by an SVD-based least-squares solve (LAPACK `dgelsd`) with relative threshold $\varepsilon_{\text{rcond}}$. Here $\varepsilon_{\text{rcond}}$ is the relative cutoff below which singular values are treated as zero in the truncated-SVD solve: a direction of the moment matrix whose singular value σ falls below $\varepsilon_{\text{rcond}}\,\sigma_{\max}$, with $\sigma_{\max}$ the largest singular value of that matrix, is discarded, which regularizes the inversion of the modal coefficients against round-off-level rank deficiency. We set $\varepsilon_{\text{rcond}} = 10^{-14}$, just above double-precision machine epsilon, so that only numerically negligible directions are removed and the full spectral richness of the outgoing basis is retained. This threshold does not by itself govern the stability of the updating operators: the conditioning of the moment matrix is controlled primarily by the wavenumber sampling Δk, and the non-amplification of $\mathbf{G}^{(i)}$ is enforced by the joint $(\Delta k, \Delta t)$ calibration through the Frobenius-norm criterion of Section 5.2. A larger $\varepsilon_{\text{rcond}}$ would truncate additional near-degenerate modes, lowering the operator norm at the expense of far-field accuracy; the present value favors accuracy, with any residual amplification kept below unity by the calibration.

Data availability

No data was used for the research described in the article.

References

[1] Silling SA. Reformulation of elasticity theory for discontinuities and long-range forces. J Mech Phys Solids 2000;48(1):175–209.
[2] Silling SA, Askari E. A meshfree method based on the peridynamic model of solid mechanics. Comput Struct 2005;83(17–18):1526–35.
[3] Silling SA, Epton M, Weckner O, Xu J, Askari E. Peridynamic states and constitutive modeling. J Elasticity 2007;88(2):151–84.
[4] Silling SA. Linearized theory of peridynamic states. J Elasticity 2010;99(1):85–111.
[5] Abadi MK, Kabir MZ. A novel rotational spring model to enrich the ordinary state-based peridynamic method with bond rotation and elastic-plastic effects in steel plates. Eng Anal Bound Elem 2025;179:106378.
[6] Qi J, Li C, Tie Y, Zheng Y, Duan Y. An ordinary state-based peridynamics modeling method for simulating anchor bolt pullout in concrete. Eng Anal Bound Elem 2024;166:105810.
[7] Wang G, He W, Lu D, Song Z, Du X. A peridynamic method for creep and stress relaxation incorporating a novel fractional viscoelastic model. Eng Anal Bound Elem 2025;171:106104.
[8] Engquist B, Majda A. Absorbing boundary conditions for the numerical simulation of waves. Math Comp 1977;31(139):629–51.
[9] Givoli D. High-order local non-reflecting boundary conditions: a review. Wave Motion 2004;39(4):319–26.
[10] Shojaei A, Mossaiby F, Zaccariotto M, Galvanetto U. A local collocation method to construct Dirichlet-type absorbing boundary conditions for transient scalar wave propagation problems. Comput Methods Appl Mech Engrg 2019;356:629–51.
[11] Mossaiby F, Shojaei A, Boroomand B, Zaccariotto M, Galvanetto U. Local Dirichlet-type absorbing boundary conditions for transient elastic wave propagation problems. Comput Methods Appl Mech Engrg 2020;362:112856.
[12] Ma H, Tian A, Sui G, Li Q, Zhang Y. Analysis of acoustic radiation problems involving arbitrary immersed media interfaces by the extended finite element method with Dirichlet to Neumann boundary condition. Eng Anal Bound Elem 2024;168:105936.
[13] Berenger J-P. A perfectly matched layer for the absorption of electromagnetic waves. J Comput Phys 1994;114(2):185–200.
[14] Zhang J, Zhao M, Zhang G, Zhang J, Du X. 3D acoustic scaled boundary perfectly matched layer (SBPML) for acoustic-structure interaction problems. Eng Anal Bound Elem 2024;164:105765.
[15] Le Q, Bobaru F. Surface corrections for peridynamic models in elasticity and fracture. Comput Mech 2018;61(4):499–518.
[16] Liu Y, Han F, Zhang L. An extended fictitious node method for surface effect correction of bond-based peridynamics. Eng Anal Bound Elem 2022;143:78–94.
[17] Shojaei A, Ongaro G, Hermann A, Silling SA, Trovalusci P, Cyron CJ. Surface and boundary corrections in peridynamics using optimized nodal influence weights. Internat J Numer Methods Engrg 2026;127(14):e70385.
[18] Zhang W, Yang J, Zhang J, Du Q. Artificial boundary conditions for nonlocal heat equations on unbounded domain. Commun Comput Phys 2017;21(1):16–39.
[19] Shojaei A, Hermann A, Seleson P, Silling SA, Rabczuk T, Cyron CJ. Peridynamic elastic waves in two-dimensional unbounded domains: Construction of nonlocal Dirichlet-type absorbing boundary conditions. Comput Methods Appl Mech Engrg 2023;407:115948.
[20] Hermann A, Shojaei A, Seleson P, Cyron CJ, Silling SA. Dirichlet-type absorbing boundary conditions for peridynamic scalar waves in two-dimensional viscous media. Internat J Numer Methods Engrg 2023;124(16):3524–53.
[21] Wildman RA, Gazonas GA. A finite difference-augmented peridynamics method for reducing wave dispersion. Int J Fract 2014;190(1):39–52.
[22] Wildman RA, Gazonas GA. A perfectly matched layer for peridynamics in two dimensions. J Mech Mater Struct 2013;7(8):765–81.
[23] Pang G, Ji S, Antoine X. Accurate absorbing boundary conditions for two-dimensional peridynamics. J Comput Phys 2022;466:111351.
[24] Shojaei A, Hermann A, Seleson P, Cyron CJ. Dirichlet absorbing boundary conditions for classical and peridynamic diffusion-type models. Comput Mech 2020;66(4):773–93.
[25] Shojaei A, Hermann A, Cyron CJ, Seleson P, Silling SA. A hybrid meshfree discretization to improve the numerical performance of peridynamic models. Comput Methods Appl Mech Engrg 2022;391:114544.
[26] Ongaro G, Shojaei A, Mossaiby F, Hermann A, Cyron CJ, Trovalusci P. Multi-adaptive spatial discretization of bond-based peridynamics: G. Ongaro et al. Int J Fract 2023;244(1):1–24.
[27] Sotudeh M, Mossaiby F, Shojaei A. On efficient numerical integration for peridynamic modeling. Comput Mech 2025;76(6):1659–87.
[28] Yu K, Xin X, Lease K. A new adaptive integration method for the peridynamic theory. Modelling Simul Mater Sci Eng 2011;19(4):045003.
[29] Mossaiby F, Häfner G, Shojaei A, Hermann A, Cyron C, Müller M, Silling S. On efficient simulation of self-assembling diblock copolymers using a peridynamic-enhanced Fourier spectral method. Comput Methods Appl Mech Engrg 2025;439:117878.
[30] Bažant ZP, Luo W, Chau VT, Bessa MA. Wave dispersion and basic concepts of peridynamics compared to classical nonlocal damage models. J Appl Mech 2016;83(11):111004.
[31] Shojaei A, Boroomand B, Mossaiby F. A simple meshless method for challenging engineering problems. Eng Comput 2015;32(6):1567–600.
[32] Shojaei A, Galvanetto U, Rabczuk T, Jenabi A, Zaccariotto M. A generalized finite difference method based on the peridynamic differential operator for the solution of problems in bounded and unbounded domains. Comput Methods Appl Mech Engrg 2019;343:100–26.
[33] Hermann A, Shojaei A, Cyron CJ. Dirichlet-type absorbing boundary conditions for ordinary state-based peridynamics. 2026, http://dx.doi.org/10.5281/zenodo.19110570.
[34] Horn RA, Johnson CR. Matrix Analysis. second ed. Cambridge: Cambridge University Press; 2013.
[35] Golub GH, Van Loan CF. Matrix Computations. fourth ed. Baltimore, MD: Johns Hopkins University Press; 2013.